



Cite this: *Phys. Chem. Chem. Phys.*, 2021, 23, 19435

Coarse-grained simulations of ionic liquid materials: from monomeric ionic liquids to ionic liquid crystals and polymeric ionic liquids[†]

Yong-Lei Wang, ^{*a} Bin Li, ^b and Aatto Laaksonen^{acde}

Ionic liquid (IL) materials are promising electrolytes with striking physicochemical properties for energy and environmental applications. Heterogeneous structures and transport quantities of monomeric and polymeric ILs are intrinsically intercorrelated and span multiple spatiotemporal scales, which is more feasible for coarse-grained (CG) simulations than atomistic modelling. Herein we constructed a novel CG model for ethyl-imidazolium tetrafluoroborate ILs with varied cation alkyl chains ranging from C₂ to C₂₀, and the interaction parameters were validated against representative static and dynamic properties that were obtained from atomistic reference simulations and experimental characterizations at relevant thermodynamic states. This CG model was extended to study thermotropic phase behaviors of monomeric ILs and to explore ion association structures and ion transport quantities in polymeric ILs with different architectures. A systematic analysis of structural and dynamical quantities identifies an evolution of liquid morphology from homogeneous to nanosegregated structures and then a smectic mesomorphism *via* a gradual lengthening of cation alkyl chains, and thereafter a distinct structural transition characterized by a monotonic decrease in orientational and translational order parameters in a sequential heating cascade. Backbone and pendant polymeric ILs exhibit evident anion association structures with cation monomers and polymer chains, and striking intra- and interchain coordinations between cation monomers owing to an intrinsic polymer architecture effect. Such a peculiar ion pairing association leads to a progressive increase in anion intrachain hopping probabilities, and a concomitant decrease in anion interchain hopping events with a gradual lengthening of polymeric ILs. The anion diffusivities in polymeric ILs are intrinsically correlated with ion pairing association lifetimes and ion structural relaxation times *via* a universal power law correlation $D \sim \tau^{-1}$, irrespective of polymer architectures.

Received 13th June 2021,
Accepted 13th August 2021

DOI: 10.1039/d1cp02662c

rsc.li/pccp

^a Department of Materials and Environmental Chemistry, Arrhenius Laboratory, Stockholm University, SE-10691 Stockholm, Sweden. E-mail: wangyol@gmail.com

^b School of Chemical Engineering and Technology, Sun Yat-sen University, Zhuhai 519082, P. R. China

^c State Key Laboratory of Materials-Oriented and Chemical Engineering, Nanjing Tech University, Nanjing 210009, P. R. China

^d Centre of Advanced Research in Bionanoconjugates and Biopolymers, Petru Poni Institute of Macromolecular Chemistry, Aleea Grigore Ghica-Voda, 41A, 700487 Iasi, Romania

^e Department of Engineering Sciences and Mathematics, Division of Energy Science, Luleå University of Technology, SE-97187 Luleå, Sweden

[†] Electronic supplementary information (ESI) available. See DOI: 10.1039/d1cp02662c

[‡] These authors contributed equally to this work.

[§] Present address: Department of Electrochemical Energy Storage, Helmholtz-Zentrum Berlin für Materialien und Energie, Hahn-Meitner-Platz 1, 14109 Berlin, Germany.

I. Introduction

Ionic liquids (ILs) are an emerging class of molten salts entirely composed of bulky organic cations and weakly coordinating anions with their melting points below 100 °C.^{1–4} Recent years have seen a great enthusiasm for imidazolium-based ILs regarding their utilities as fascinating functional materials in diverse applications ranging from material synthesis and catalysis to gas adsorption and separation, electrotunable lubrication and tribology, and electrochemical devices for energy storage and harvesting.^{5–9} These promising applications of imidazolium ILs are mainly attributed to multifaceted physicochemical characteristics of ILs, such as nonflammability and negligible volatility, reasonable viscosity-conductivity features, high electrochemical- and thermal-oxidative stabilities, wide electrochemical windows, and exceptional affinities to molecular compounds having varied polarities.^{1–5} These remarkable properties of imidazolium ILs are intrinsically correlated with inherent ion structures

and delicate intra- and intermolecular interactions ranging from weak, isotropic and nonspecific forces to strong, anisotropic and specific forces among constituent ions.^{2–4} Additionally, these fascinating quantities can be widely tuned in a controllable fashion *via* a judicious selection of cation–anion moieties and by mutating specific atoms in constituent ions, leading to the formation of remarkable liquid structures and endowing imidazolium ILs with abundant phase behaviors.^{4,10–14}



Yong-Lei Wang

currently a research scientist at Helmholtz-Zentrum Berlin for Materials and Energy and a guest researcher at Stockholm University. His research interests include numerical algorithm development for efficient handling of long-range coulombic interactions, multiscale modelling of ionic fluids and polymeric electrolyte materials in electrochemical devices, and computational studies of luminescent properties of transition-metal complexes in biological systems.

Yong-Lei Wang received his PhD degree in Physical Chemistry from Jilin University (2012) and Stockholm University (2013). Thereafter, he worked as a postdoctoral research fellow at Stockholm University and KTH Royal Institute of Technology. He received financial support from Knut and Alice Wallenberg Foundation in 2016 and worked as a Wallenberg Fellow at Stanford University and Stockholm University. He is

Both experimental and computational studies have demonstrated that imidazolium ILs can form segregated liquid organization at nanoscopic level when cation alkyl chains are longer than C₄. This is intrinsically attributed to electrostatic interactions among charged species which force cation alkyl chains and other hydrophobic groups to aggregate and form apolar domains that are either segregated or interpenetrated with polar network in IL matrices.^{2,4,15–18} Furthermore, the dispersion associations among apolar units increase with lengthening cation alkyl chains, and when cation alkyl chains are adequately long, the strength of their preferential dispersion interactions facilitates the alignment of alkyl chains in parallel and the formation of peculiar ionic liquid crystalline (ILC) phase that has unique features beyond traditional liquid crystals.^{12,13,19,20} Applications of imidazolium ILCs are mainly concentrated on their anisotropic ion transport properties as they are promising electrolyte materials for electrochemical applications.^{5,7,13,14,21}

The macroscopic functionalities of imidazolium ILs can be further expanded *via* polymerization of imidazolium cations.^{22–25} The imidazolium-based poly(ionic liquid)s (PILs), either backbone or pendant type, present additional promising characteristics, such as high electrochemical and mechanical stabilities, and distinct ion transport quantities compared with monomeric ILs.^{26–32} These intrinsic characteristics of PILs have triggered significant enthusiasm in the pursuit of polyelectrolyte materials possessing an optimal combination of mechanical strength, ion conductivity, and transference number for a wide range of energy storage and conversion applications.^{5,7,24,25} In contrast to extensive experimental and computational characterizations of physicochemical properties of pure ILs and IL-based mixtures, there are sporadic investigations concerning these quantities of PILs and salt-doped PIL materials. Recent



Bin Li

focuses on molecular simulations of soft matter systems, including ionic liquids, and self-assembly of polymers and colloids.

Bin Li received his PhD from Institute of Theoretical Chemistry, Jilin University, with Prof. Zhong-Yuan Lu in 2013. After the research careers in Technical University of Darmstadt, Germany, Lund University, Sweden, and National Center for Nanoscience and Technology, China, currently he is an assistant professor at School of Chemical Engineering and Technology, Sun Yat-sen University, China. He mainly



Aatto Laaksonen

Aatto Laaksonen: Fil.kand. (Major in Mathematics) Stockholm University (SU) 1976, PhD in Quantum Chemistry (SU) 1981, PDF: Daresbury Laboratory (UK) 1982 with Victor Saunders, IBM Kingston Laboratories (USA) 1983–1985 with Enrico Clementi. Docent (habilitation) in Physical Chemistry (SU) 1984, Professor of Physical Chemistry (SU) 2000. Sabbatical at Dalhousie University (Canada) 1993–1994 & 1995 with Rod Wasylishen, Visiting professor at Japan Atomic Energy Research Institute 2002, 2005, Cagliari University Italy 2011, 2012, 2013, 2015, Nanyang Technological University, Singapore, 2017. Nanjing Tech, PRC, 2019 & 2020. STIAS Fellow (Stellenbosch Institute of Advanced Study), South Africa 2014. Main research areas: multi-scale modeling (from Materials/nano Science to Biopharma) and green Chemical Engineering.

experimental studies reported significant deviation in the dependency of ion conductivity from polymer segmental dynamics,^{27,28,33–35} and subsequent atomistic simulations^{30,32,36} demonstrated that anion mobility in PILs occurs *via* a combination of intra- and interchain ion hopping events through the formation and breaking of ion association structures between anions and PIL cation monomers. This feature is substantially different to transport quantities of anions in monomeric ILs, where anion diffusion is closely correlated with structural relaxation of surrounding ionic medium.^{4,11,37} Such a discrepancy was suggested to be the main origin of experimental observation in which long PILs exhibit higher ion conductivity than short PILs and monomeric ILs when compared at the same glass-transition-normalized temperature.³⁸ The decoupling of ion transport quantities from segmental dynamics of PILs is essentially correlated with microstructures and mesoscopic morphologies of PILs, as revealed from recent multiscale modelling of imidazolium PILs consisting of varied anion moieties.^{5,29,36} This leads to complicated microstructural relaxations and the corresponding lifetimes spanning multiple temporal scales for ion association, ion hopping and diffusion,^{4,39–41} and spatial rearrangements of polar and apolar domains in bulk materials and in selective solvents.^{42,43} In this regard, multiscale modelling of monomeric IL and PIL materials combining all-atomistic (AA) and coarse-grained (CG) simulations is a promising procedure to explore complex phase behaviors of these ion-containing materials at extended spatiotemporal scales with a modest computational cost.^{3,4,44–48}

Roy and coworkers proposed an idealized four-site CG model having characteristics resembling those of 1-butyl-3-methylimidazolium hexafluorophosphate ($[C_1C_4IM][PF_6]$) IL for simulating solvation dynamics and charge transfer phenomena on microsecond time scale.⁴⁹ The adopted coarse-graining strategy is similar in spirit to CG models for imidazolium ILs developed by Wang *et al.*^{15,44,50} and Karimi-Varzaneh *et al.*⁵¹ for studying aggregation structures of polar and apolar domains and ensuing dynamical quantities in heterogeneous IL matrices. The derived interaction parameters for CG beads were able to reproduce structural and energetic properties of a prototypical $[C_1C_4IM][PF_6]$ IL but with slaved transport quantities at a wide temperature range, which could be significantly improved *via* a rescaling of ion charges.⁵² Such a CG representation was adapted by Merlet and coworkers to explore capacitive properties of ILs used as electrolyte materials in electrochemical devices.^{53–56}

Besides these CG representations, we made endeavors in previous studies to develop CG models for ILs consisting of imidazolium cations coupled with spherical anions.^{48,57} Instead of using analytical functions representing intermolecular interactions between CG beads, we derived tabulated potentials from reference radial distribution functions that were calculated from underlying AA MD simulations using the Newton Inversion and iterative Boltzmann Inversion methods.^{51,58} The developed CG models were further calibrated so as to capture essential physicochemical and structural features, and solute-based dynamics of model ionic fluids over a wide temperature

range while being simple enough to be computationally economical.⁴⁸

It should be particularly mentioned that these proposed CG models have been widely used to study static and dynamic quantities of isotropic phase of imidazolium ILs having short cation alkyl chains, and are rarely used to explore relevant properties of ILCs and PILs, as well as their functionalities in promising applications, due to limited transferability of these CG models in describing phase behaviors of ILs having long alkyl chains and of PILs with different polymer architectures. In the current work, following the parametrization strategy used in Bresme's work,⁵⁹ we first adopt the coarse-graining scheme to construct CG model for 1-alkyl-3-ethylimidazolium tetrafluoroborate ($[C_2C_nIM][BF_4]$) ILs, and thereafter calibrate interaction parameters against representative thermodynamics, structural, and dynamic properties that were obtained from reference AA MD simulations and experimental characterizations at relevant thermodynamic states. The constructed CG model for $[C_2C_nIM][BF_4]$ ILs and the derived effective interaction parameters between CG beads are extended to study thermotropic phase behaviors of monomeric ILs and to explore ion association structures and ion transport quantities in PILs with different architectures at extended spatiotemporal scales.

II. Description of coarse-grained model and validation of interaction parameters

A. The CG model for $[C_2C_nIM][BF_4]$ ILs

The CG model for $[C_2C_nIM][BF_4]$ ILs is constructed with the following principles: the planar imidazolium ring is represented by a single bead tagged as "IM" carrying a partial charge of $+1.0e$; the $[BF_4]$ anion is mapped into a single CG bead labelled as "BF" carrying a partial charge of $-1.0e$; each ethyl or ethylene unit is coarsened into one neutral CG bead, in which the head and tail beads are labelled as "CH" and "CT", respectively, and the others are termed as "CE" for convenience of discussion (all these neutral CG beads have the same set of interaction parameters). Such a mapping scheme for a representative $[C_2C_4IM][BF_4]$ is illustrated in Fig. 1. The relative positions of these CG beads are determined from the center-of-mass of the corresponding atomistic units. It is noted that such a constructed CG model is compatible with that developed in previous studies for methyl-imidazolium ILs coupled with varied anion species,^{44,46–51,53,54,60} and exhibit considerable transferability to triazolium-based ILs.⁶¹

The bonded interactions between CG beads consisting of bond stretching, angle bending and dihedral terms have a similar form with those for the corresponding atomistic models but with different force constant parameters, which were originally taken from previous works,^{48,59} and thereafter calibrated to reproduce probability distributions of bond lengths, angles, and dihedrals that were extracted from extensive atomistic reference simulations of $[C_2C_nIM][BF_4]$ ILs at different thermodynamic states. The interaction potential forms, the

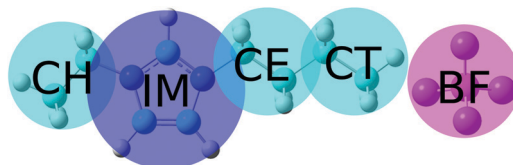


Fig. 1 Coarse-graining scheme for $[C_2C_4IM][BF_4]$. The blue and magenta spheres are labelled as “IM” and “BF” representing positively charged imidazolium ring and negatively charged $[BF_4]$ anion with partial charges of $+1.0e$ and $-1.0e$, respectively. The cyan beads representing ethyl and ethylene units in atomistic models are neutral spheres having the same set of interaction parameters. Herein the head and tail ethyl units are labelled as “CH” and “CT”, respectively, and the others are termed as “CE” for convenience of discussion. The CH and CT beads are specifically highlighted with different colors in relevant subsections to address their distributions in modelling systems.

determined interaction parameters for constructed CG model for $[C_2C_nIM][BF_4]$ ILs, and AA and CG MD simulation protocols are provided in the ESI.[†]

B. Structural properties and liquid organizations

Fig. 2 presents a comprehensive comparison of probability distributions of bond lengths, angles, and dihedrals among CG beads obtained from CG MD simulations with those determined from reference atomistic modelling systems at relevant thermodynamic states. It is clearly illustrated that probability distributions of bond lengths and angles are quantitatively

reproduced from CG MD simulations. The marginal discrepancy between AA and CG MD simulations of CE-CE(CT) bond length (Fig. 2(c)) and CE-CE-CE(CT) angle distribution (Fig. 2(f)) is mainly attributed to dihedral preference and constrained distribution of C-H bonds having *gauche* and *trans* configurations around C-C bond in the ethyl group in atomistic model, which are totally averaged out in the simplified CG model, leading to the smooth distribution of CE-CE(CT) bond length and CE-CE-CE(CT) angle obtained from CG MD simulations. The bimodal feature in probability distributions for CH-IM-CE-CE(CT) and IM-CE-CE-CE dihedrals and the flat arch character for CE-CE-CE(CT) dihedral distributions determined from the constructed CG model exhibit qualitative agreement with that calculated from reference AA MD simulations.

The intermolecular structures of CG beads are quantified *via* the calculation of site–site radial distribution functions (RDFs) to concrete their specific spatial correlations in heterogeneous IL matrices. Fig. 3 presents representative RDFs for CG bead pairs, and these RDFs are compared with their counterparts determined from atomistic reference simulations at similar thermodynamic states. Both peak positions and plot shapes of reference RDFs determined from atomistic simulations are well reproduced from CG MD simulations, indicating that the constructed CG model and the calibrated interaction parameters can essentially retain local ion structures in $[C_2C_nIM][BF_4]$ ILs having different cation alkyl chains. The IM-IM pair RDFs (Fig. 3(a)) exhibit considerably short-ranged

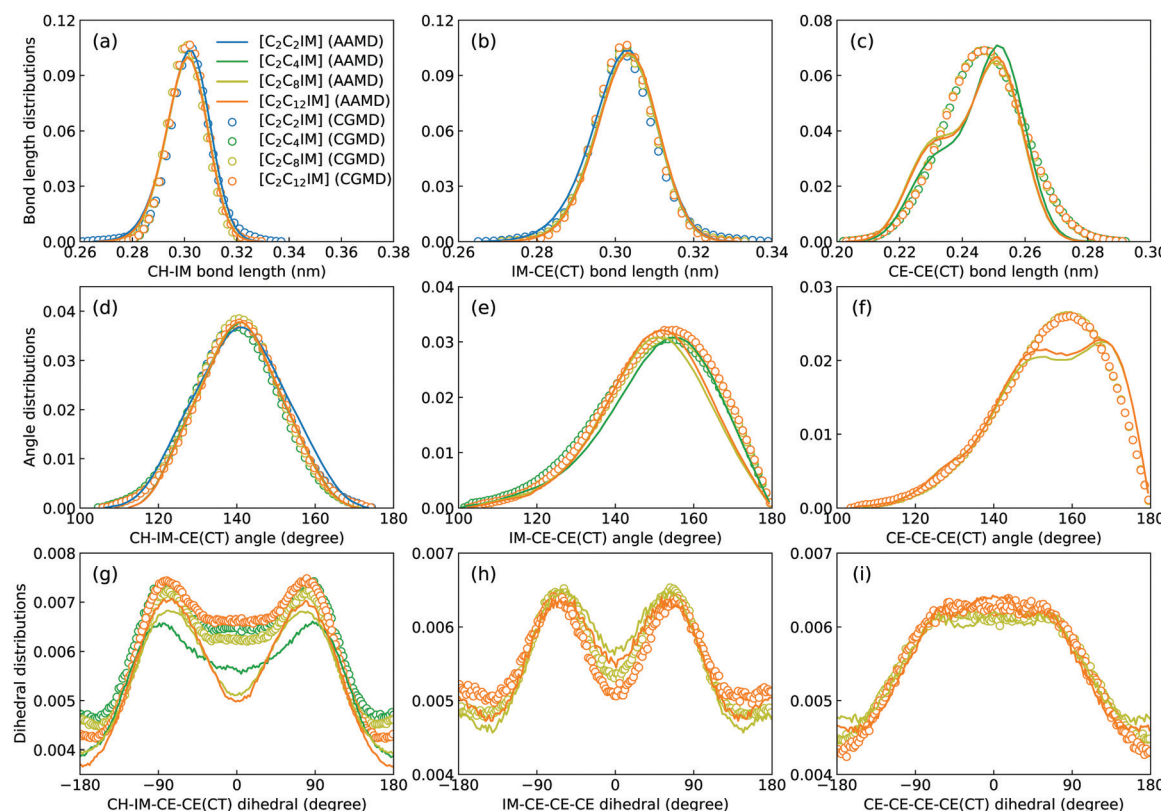


Fig. 2 Probability distributions of bond lengths (top panels), angles (middle panels), and dihedrals (bottom panels) for $[C_2C_nIM][BF_4]$ ILs obtained from CG MD simulations compared with those determined from atomistic reference simulations at 400 K.

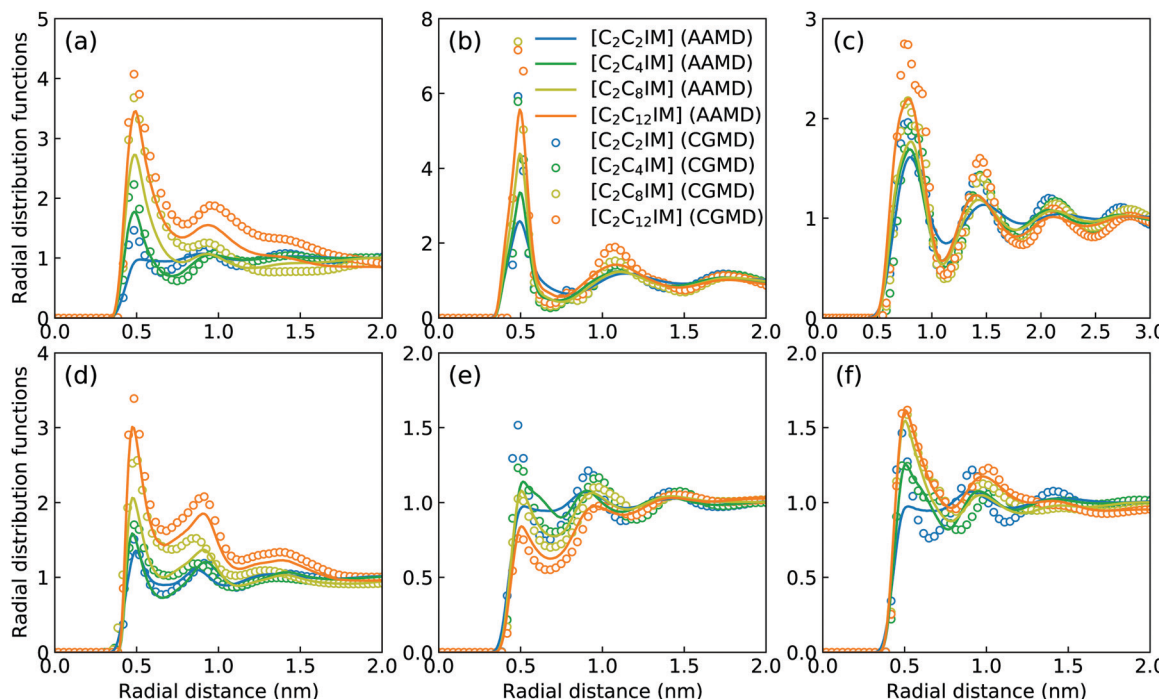


Fig. 3 Representative radial distribution functions of (a) IM–IM, (b) IM–BF, (c) BF–BF, (d) CH–CH, (e) CH–CE(CT), and (f) CE(CT)–CE(CT) pairs for $[C_2C_nIM][BF_4]$ ILs obtained from reference AA and CG MD simulations performed at 400 K.

correlations, which are comparable with those for CH–CH pair RDFs (Fig. 3(d)) due to their intrinsic positions in cation framework. The existence of multiple secondary peaks in IM–BF (Fig. 3(b)) and BF–BF (Fig. 3(c)) pair RDFs indicates strong structural correlations among these charged beads *via* electrostatic interactions, which is an intrinsic characteristic of a model system dominated by coulombic interactions among charged species. These ion-related structures in IL matrices have an impact on the number of counterions present in solvation shells of a given ion, and an even significant effect on spatial distributions of ions with like charges nearby.

It should be noted that there are marginal variations of peak intensities and peak positions in RDF plots obtained from CG MD simulations compared with those determined from atomistic reference simulations, which can be essentially rationalized by the simplification of atomistic model for $[C_2C_nIM][BF_4]$ ILs and the absence of some conformational constraints in the developed CG model for $[C_2C_nIM]$ cations.^{44,46,48,49,54,59} In fact, these disparities can be minimized with a gradual lengthening of cation alkyl chains from C_4 to C_{12} , indicating that the constructed CG model and the derived interaction parameters for CG beads are effective in predicting microstructures of reference atomistic modelling systems at different thermodynamic states.

The evolution of microstructures in $[C_2C_nIM][BF_4]$ ILs with a gradual lengthening of cation alkyl chains is visualized by representative snapshots in Fig. 4, and is rationalized by competitive associations between preferential electrostatic interactions among charged beads and collective solvophobic coordinations among neutral beads.^{15,49,51,57} For ILs consisting

of short cation alkyl chains, such as $[C_2C_2IM][BF_4]$ (Fig. 4(a)) and $[C_2C_4IM][BF_4]$ (Fig. 4(b)), the mesoscopic liquid structures are characterized by homogeneous distributions of CG beads in IL matrices. A progressive lengthening of cation alkyl chains leads to an aggregation of neutral beads and the formation of apolar domains owing to their mutual solvophobic characteristics.^{15,49,57} For ILs consisting of intermediate cation alkyl chains, like $[C_2C_8IM][BF_4]$ (Fig. 4(c)), the mesoscopic liquid structures are described by bi-continuous sponge-like arrangements of interpenetrating polar and apolar networks. The further lengthening of cation alkyl chains leads to a significant permeation of polar network by expanded apolar domains, the former of which tends to persist but has to accommodate the growing apolar domains by loosing part of its connectivity in IL matrices, resulting in the segregation of polar domains within apolar framework. These computational results obtained from CG MD simulations using a simplified ion model are in qualitative agreement with experimental observations in characterizing variations of microstructures and liquid organizations of imidazolium ILs with a progressive lengthening of cation alkyl chains.^{16–18}

The charge ordering phenomena in IL matrices can be quantified using a charge distribution function, $Q_i(r)$, which is defined such that $4\pi r^2 q_i Q_i(r) dr$ is the net charge from a central ion i located at r_i having a partial charge q_i . The total charge distribution function can be obtained by a summation of partial charge distribution functions for $[C_2C_nIM]$ cations (Q^{CA}) and $[BF_4]$ anions (Q^{AN}) *via* $Q(r) = Q^{CA}(r) + Q^{AN}(r)$, in which Q^{CA} and Q^{AN} are correlated with RDFs among charged beads through $Q^{CA}(r) = \rho(g^{CA-CA}(r) - g^{CA-AN}(r))$ and

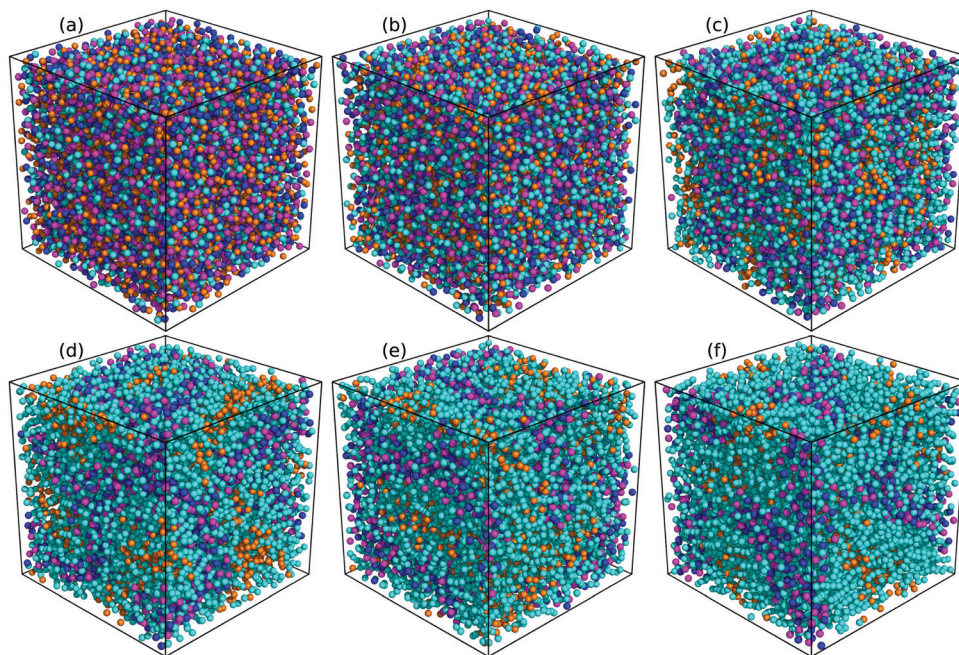


Fig. 4 Representative liquid morphologies of (a) $[C_2C_2IM][BF_4]$, (b) $[C_2C_4IM][BF_4]$, (c) $[C_2C_8IM][BF_4]$, (d) $[C_2C_{12}IM][BF_4]$, (e) $[C_2C_{16}IM][BF_4]$, and (f) $[C_2C_{20}IM][BF_4]$ ILs at 400 K. The color codes of these CG beads are the same as those shown in Fig. 1 except that the tail CT beads in $[C_2C_nIM]$ cations are highlighted with orange spheres to visualize their distinct distributions in apolar domains in IL matrices.

$Q^{AN}(r) = \rho(g^{AN-AN}(r) - g^{CA-AN}(r))$, respectively.^{46,57} $\rho = \rho^{CA} + \rho^{AN}$ is the total number density of charged beads in CG modelling systems. Fig. 5(a) presents the total charge distribution functions for $[C_2C_nIM][BF_4]$ ILs calculated from reference AA and CG MD simulations. Charge oscillations are strongly damped in all studied IL matrices, indicating that these modelling systems exhibit striking charge ordering phenomenon.

Such a charge ordering phenomenon in modelling systems dominated by coulombic interactions among charge beads can be quantified *via* fitting charge distribution functions to an asymptotic form $Q(r) = \frac{A}{r} e^{-r/\lambda_{IL}} \sin\left(\frac{2\pi r}{d} + \phi\right)$, in which the parameter of interest is the charge screening length (λ_{IL})

quantifying a distance beyond which the local charge neutrality is achieved in bulk liquid region.^{46,62} The estimated charge screening lengths λ_{IL} for $[C_2C_nIM][BF_4]$ ILs, as shown in Fig. 5(b), demonstrate that the constructed CG model and the derived interaction parameters can generate consistent results with those obtained from atomistic reference simulations. In addition, these computational results are comparable with those for $[C_1C_nIM][PF_6]$ ILs obtained by Moradzadeh *et al.* if we ignore the marginal difference between $[BF_4]$ and $[PF_6]$ anions.^{46,49,57} The charge screening length data for $[C_2C_nIM][BF_4]$ and $[C_1C_nIM][PF_6]$ ILs decrease with lengthening cation alkyl chains, which is expected due to enhanced microstructural heterogeneities in modelling systems that are

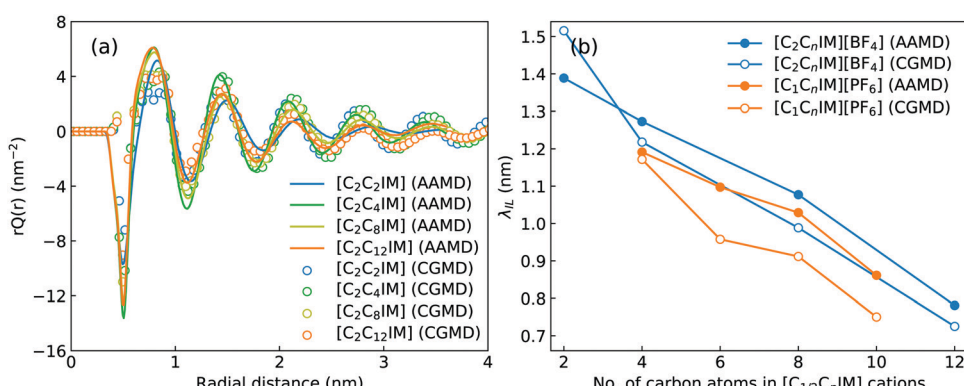


Fig. 5 (a) Charge distribution functions for $[C_2C_nIM][BF_4]$ ILs calculated from AA and CG MD simulations, and (b) charge screening lengths of electrostatic correlations for $[C_2C_nIM][BF_4]$ ILs with varied cation alkyl chains. The charge screening length data for $[C_1C_nIM][PF_6]$ ILs are taken from ref. 46 for a comparative purpose.

originated from competitive associations between electrostatic interactions among charged beads and solvophobic forces among neutral spheres.

C. Thermodynamic and dynamic quantities of $[C_2C_nIM][BF_4]$ ILs

Besides the reproduction of microstructures of atomistic reference modelling systems, the constructed CG model and the derived interaction parameters can produce a reasonable linear scaling of liquid densities of $[C_2C_nIM][BF_4]$ ILs against temperatures. It is noted that there are limited density data for $[C_2C_nIM][BF_4]$ ILs, and therefore we provide experimental density data for $[C_1C_mIM][BF_4]$ ILs for a comparative propose. It is shown in Fig. 6 that the temperature-dependent liquid densities of $[C_2C_nIM][BF_4]$ ILs are consistent with those determined from experimental measurements^{63–65} with a maximum uncertainty of 3.5%. The slopes of these computational density data against temperatures are thermal expansion coefficients, which generally fall within the range for typical imidazolium ILs obtained from numerous experimental measurements and computational calculations.^{46,49,51,57}

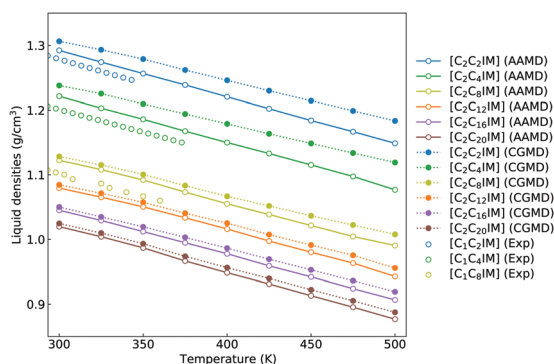
It should be further noted that the constructed CG model and the derived interaction parameters exhibit a good transferability and representability in generating consistent microstructural and thermodynamic quantities (provided in the ESI†) of triazolium ILs.⁶¹ Therefore it is expected that this model can be used as a generic bead-spring model to explore phase behaviors of imidazolium and triazolium ILs, and even ion groups bearing heteroaromatic ring planes at varied thermodynamic conditions.

To go beyond microstructures and thermodynamic properties, we examine translational and rotational dynamics of $[C_2C_nIM]$ cations at a wide temperature range to explore the dependence of these dynamic quantities on alkyl chain lengths and temperatures in bulk IL matrices. The diffusion coefficients of $[C_2C_nIM]$ cations and $[BF_4]$ anions determined from mean square displacements in AA and CG MD simulations are shown in Fig. 7, and these computational data are compared with relevant experimental data.⁶⁶ The diffusion coefficients of $[C_2C_nIM]$ cations and $[BF_4]$ anions fall within the order of

$10^{-12}\text{--}10^{-8}\text{ m}^2\text{ s}^{-1}$ at 300–500 K, which is consistent with computational results obtained from previous studies using varied CG models.^{46,48,49,51,54,59} In addition, the diffusion coefficients determined from CG MD simulations are larger than the corresponding experimental values and atomistic simulation data by a factor of 2–7, indicating that the constructed CG model and the derived interaction parameters can essentially capture temperature-dependant and alkyl chain length-dependent translational dynamics of ion species in $[C_2C_nIM][BF_4]$ ILs at a wide temperature range.

At given temperatures, the comparable mobilities of charged IM and BF beads suggest their preferential associations in local ionic domains because of electrostatic interactions,^{4,46,48,49,59} whereas the neutral tail CT beads in CG $[C_2C_nIM]$ cations exhibit the fastest translational diffusivities due to their distributions in local cavities of apolar domains, as clearly visualized in the lower panels in Fig. 4. Lengthening cation alkyl chains leads to a substantial decrease in diffusivities of $[C_2C_nIM]$ cations and $[BF_4]$ anions, which can be rationalized by a distinct evolution of mesoscopic liquid morphologies of ILs. The mobilities of CG $[C_2C_nIM]$ cations and $[BF_4]$ anions can be qualitatively sorted into three categories depending on cation alkyl chain lengths. For $[C_2C_nIM][BF_4]$ ILs with short cation alkyl chains, such as $n = 2$ and $n = 4$, the spatial distributions of ion groups in IL matrices are relatively homogeneous and there is no phase segregation of polar and apolar domains. The comparable diffusions of CG cations and anions are mainly influenced by strong electrostatic coordinations among charged beads. For cation alkyl chains longer than C_4 , the hydrophobic alkyl chains tends to aggregate and form apolar clusters, apolar domains and then interpenetrating apolar network in heterogeneous IL matrices with a gradual lengthening of cation alkyl chains. Such a striking microstructural transition leads to a significant decrease in mobilities of cations and anions, as clearly manifested in diffusion coefficient data for $[C_2C_8IM][BF_4]$, $[C_2C_{12}IM][BF_4]$ and $[C_2C_{16}IM][BF_4]$ ILs. However, the further lengthening of cation alkyl chains from C_{16} to C_{20} leads to marginal changes in microstructures and liquid morphologies. Therefore, even the translational diffusivities of ion groups in $[C_2C_{20}IM][BF_4]$ IL are considerably decreased, the magnitude of reduction is not so significant compared with that from $[C_2C_4IM][BF_4]$ to $[C_2C_{16}IM][BF_4]$ ILs.

The translational diffusivities of all CG beads and ion species exhibit an exponential increase with increasing temperatures, indicating that these temperature-dependent diffusion data can be depicted by a classic Arrhenius equation $D = D_0 e^{E_a/RT}$, where E_a is the activation energy. Fitting diffusion coefficients to the Arrhenius expression gives the activation energies of ion species, which lie within a range of 20–35 kJ mol^{−1} depending on constituent ions in modelling systems. The activation energies for charged CG beads are comparable, and are considerably larger than those for neutral beads in CG cation model, indicating that ion structures consisting of charged beads are more difficult to break in stiff ionic framework, in contrast to neutral tail beads in “soft” apolar domains.



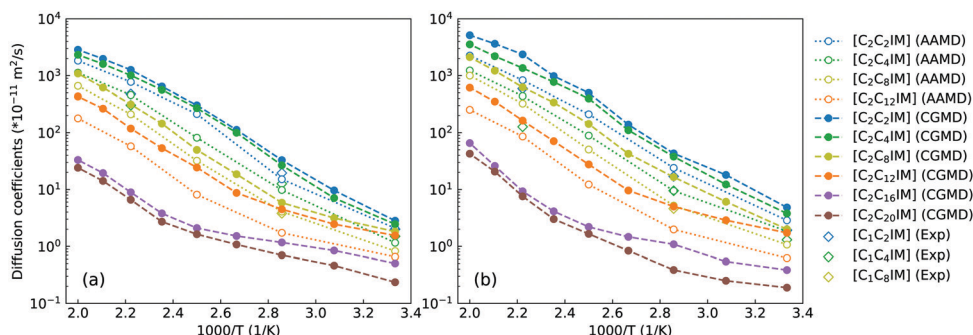


Fig. 7 Comparison of temperature-dependent translational diffusion coefficients (unit in $10^{-11} \text{ m}^2 \text{ s}^{-1}$) for (a) $[\text{C}_2\text{C}_n\text{IM}]$ cations and (b) $[\text{BF}_4]$ anions obtained from reference AA and CG MD simulations with those determined from experimental measurements for $[\text{C}_1\text{C}_m\text{IM}][\text{BF}_4]$ ($m = 2, 4$, and 8) ILs at relevant thermodynamic conditions.⁶⁶

In concert with translational dynamics, the rotational relaxations of CG $[\text{C}_2\text{C}_n\text{IM}]$ cations have been investigated by calculating the rotational correlation functions represented by the first rank Legendre polynomial $P_1(t) = \langle \hat{e}(0) \cdot \hat{e}(t) \rangle$, in which \hat{e} is a unitary vector connecting head CH and tail CT beads in CG $[\text{C}_2\text{C}_n\text{IM}]$ cations.^{32,40,41} Fig. 8 presents representative rotational correlation functions of CG $[\text{C}_2\text{C}_n\text{IM}]$ cations at different temperatures. The rotational relaxations of $[\text{C}_2\text{C}_n\text{IM}]$ cations are complicated and heterogeneous depending on the relative relaxations of charged and neutral moieties. The charged moieties are locally liberated in ion cages in polar region while neutral moieties freely swing in solvophobic domains, and additionally, a gradual lengthening of cation alkyl chains slows down rotational relaxations of $[\text{C}_2\text{C}_n\text{IM}]$ cations, which is intrinsically correlated with cation sizes and their spatial distributions in heterogeneous IL matrices. This is compatible with their translational dynamics determined from AA and CG

simulations, and microstructural relaxations of ILs determined by charged and neutral probes using ultrafast vibrational spectroscopy.^{9,48,51}

It should be addressed that these asymptotic rotational correlation functions can be best fitted to a stretched bi-exponential decay function $C(t) = C_0 + C_1 e^{-t/\tau_1} + C_2 e^{-t/\tau_2}$.^{41,67} The accessible fitting parameters τ_1 and τ_2 represent two rotational modes of a rotational body, usually a slow mode and a fast mode with different rotational timescales. The detailed description of these fitting parameters was comprehensively discussed in previous works.^{41,61,67} The total rotational correlation times τ for $[\text{C}_2\text{C}_n\text{IM}]$ cations are determined by a numerical integration of the fitted functions using $\tau = \int_0^\infty C(t) dt = \frac{\int_0^{\tau_0} C(t) dt}{1 - C(\tau_0)}$. In addition, the rotational correlation times for head units (τ_{head}), represented by a vector connecting CH and IM beads, and for tail groups (τ_{tail}), described by a vector connecting the last two tail beads (IM-CT for $[\text{C}_2\text{C}_2\text{IM}]$ and CE-CT for other cations), are determined from the corresponding rotational correlation functions. The obtained rotational correlation times, as shown in Fig. 9, demonstrate distinct rotational relaxations of polar units and apolar groups in $[\text{C}_2\text{C}_n\text{IM}]$ cations. The first feature is that an increase in temperature leads to enhanced rotational dynamics with a concomitant decrease in rotational correlation times for head units and tail groups, as well as for the whole $[\text{C}_2\text{C}_n\text{IM}]$ cations. The second character is that lengthening alkyl chains in $[\text{C}_2\text{C}_n\text{IM}]$ cations leads to a substantial increase in rotational correlation times for head units and the whole cations at relevant temperatures, and a concomitant decrease in rotational correlation times for tail groups in cations.

These computational results, as we discussed in previous subsections, are intrinsically correlated with a transition of microstructures and mesoscopic liquid morphologies for $[\text{C}_2\text{C}_n\text{IM}][\text{BF}_4]$ ILs with a gradual lengthening of cation alkyl chains. For $[\text{C}_2\text{C}_2\text{IM}]$ and $[\text{C}_2\text{C}_4\text{IM}]$ cations having short alkyl chains, the head CH-IM units are strongly coupled with anions, constraining neutral CT beads in local cavities, and therefore rotational dynamics of all cations are strongly dependent on relaxations of head CH-IM units in cations. For $[\text{C}_2\text{C}_n\text{IM}]$ cations with alkyl chains longer than C_4 , the neutral beads

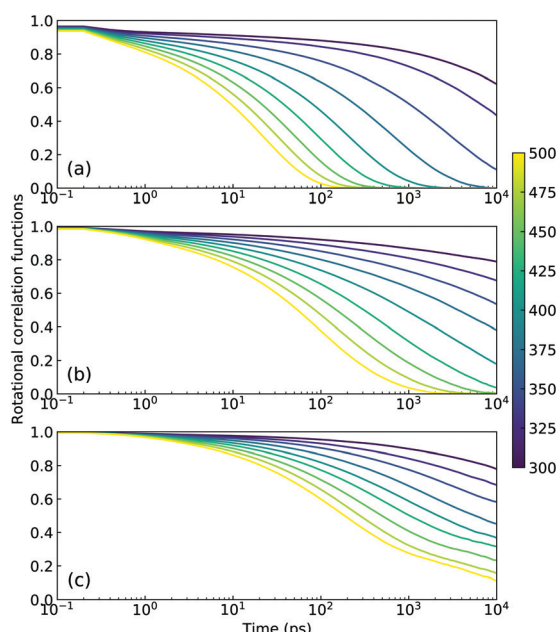


Fig. 8 Rotational correlation functions of CG (a) $[\text{C}_2\text{C}_2\text{IM}]$, (b) $[\text{C}_2\text{C}_8\text{IM}]$, and (c) $[\text{C}_2\text{C}_{16}\text{IM}]$ cations at varied temperatures.

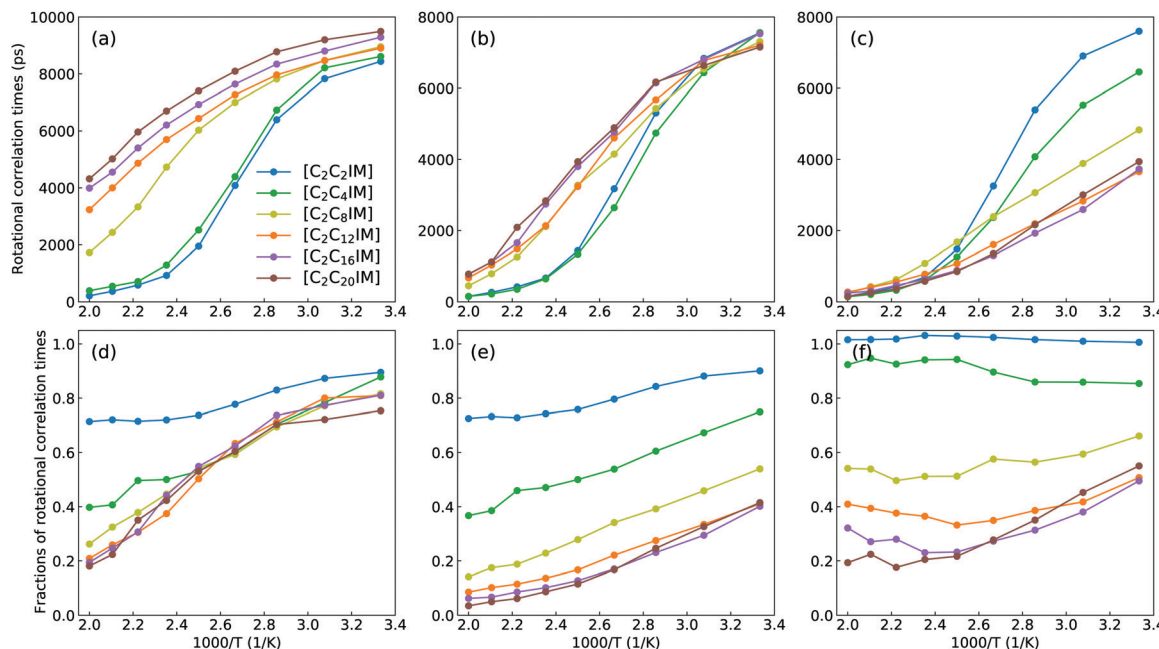


Fig. 9 Rotational correlation times of (a) $[C_2C_nIM]$ cations (τ_{cation}), (b) head CH-IM units (τ_{head}), and (c) tail (IM)CE-CT groups (τ_{tail}) in cations with varied alkyl chains, and fractions of rotational correlation times (d) $\tau_{head}/\tau_{cation}$, (e) $\tau_{tail}/\tau_{cation}$, and (f) τ_{tail}/τ_{head} for different CG cations obtained from CG MD simulations at a wide temperature range.

tend to aggregate and form apolar domains, which is highlighted by spatial distributions of neutral CT beads (orange spheres) in Fig. 4. This leads to increased rotations of tail CE-CT groups in apolar domains, and marginal changes for rotational dynamics of head CH-IM units in polar domains. It is noted that lengthening cation alkyl chains from C_{12} to C_{20} leads to a progressive increase in rotational correlation times for the whole $[C_2C_nIM]$ cations, which might be attributed to the contributions of other neutral CE beads between head CH-IM units and tail CE-CT groups in cations.

Additional physical insights for temperature-dependant and cation alkyl chain length-dependent rotational correlation times for $[C_2C_nIM]$ cations, head CH-IM units and tail (IM)CE-CT groups in cations can be obtained *via* calculating fractions of rotational correlation times for different moieties at varied temperatures shown in lower panels in Fig. 9. In $[C_2C_2IM][BF_4]$ and $[C_2C_4IM][BF_4]$ ILs, the head CH-IM units and tail (IM)CE-CT groups in cations have comparable contributions to rotational relaxations of cations. This is expected as in these two modelling systems the tail (IM)CE-CT groups are covalently bonded to head CH-IM units in cations, and therefore their rotational dynamics are strongly coupled with that for head CH-IM units in cations. For $[C_2C_nIM]$ cations with alkyl chains longer than C_8 , the contributions of head CH-IM units exhibit negligible changes, whereas tail CE-CT groups demonstrate stepwise decrease in their contributions to rotational relaxations of cations, manifesting that microstructures and spatial distributions of tail CE-CT groups in apolar domains have marginal changes in these ILs with a further lengthening of cation alkyl chains from C_8 to C_{20} . The rotational heterogeneities, embedded in charged and neutral moieties and the whole cations,

indicate that charged units are actually difficult to rotate because of a strong cation-anion association caging effect and therefore charged units have longer rotational correlation times; in contrast, neutral groups have a relatively free rotational motion due to a small energy barrier for neutral chains to rotate and diffuse in apolar domains and therefore neutral groups have shorter rotational correlation times.^{41,68-70} These two rotational modes exhibit a prevalent competitive and temperature-dependent feature in affecting the total rotational dynamics of $[C_2C_nIM]$ cations in heterogeneous IL matrices.

III. Coarse-grained simulations of ionic liquid crystalline phases

A. Phase behaviors and number density profiles

Prior investigations have established that ILs with an appropriate combination of cation alkyl chains and anion types can form striking liquid phases exhibiting ILC characteristics and long range mesoscopic ordering structures over extended temperature range.^{13,71-73} The specific combination feature for $[C_1C_nIM][BF_4]$ ILs has been experimentally determined to be $n \geq 12$.^{14,74} In addition, long alkyl chains are needed for imidazolium cations to form stable ILC structures when they are coupled with large anion groups.⁷³⁻⁷⁵ The main driving force for the formation of ILC phase, very often of smectic type mesomorphism, is the phase segregation of hydrophobic chains from ionic layers. Herein, we investigate the transferability of the constructed CG model and the derived interaction parameters in describing ILC characteristics of $[C_2C_nIM][BF_4]$ ILs at varied thermodynamic states. It should be noted that in

regular CG MD simulations the ILC structures are routinely obtained *via* annealing isotropic ILs from high to low temperatures, which, however, are highly dependent on annealing procedures, and more significantly, modelling systems are readily trapped at different metastable states.^{72,73,76-78} Therefore the transition from isotropic to crystalline structures is complicated and hardly being observed during normal simulations without enhanced sampling techniques. As such, we adopt another straightforward procedure to first generate starting configurations of IL ion pairs characterized by crystalline structures on regular lattices, and thereafter heat modelling systems to target temperatures and perform full equilibrations before taking statistical analysis.

Three model ILs, $[C_2C_4IM][BF_4]$, $[C_2C_{12}IM][BF_4]$ and $[C_2C_{20}IM][BF_4]$, are selected to explore ILC characteristics of $[C_2C_nIM][BF_4]$ ILs with short, intermediate, and long cation alkyl chains. Fig. 10 presents representative configurations of CG $[C_2C_{12}IM][BF_4]$ ILs in equilibrated simulation systems in a sequential heating cascade from 50 to 500 K. A generic smectic phase is identified and IL microstructures are much ordered at lower temperatures (<350 K) than those at higher temperatures (>350 K). The equilibrated ion structures of $[C_2C_4IM][BF_4]$ and $[C_2C_{20}IM][BF_4]$ ILs (provided in ESI†), and ensuing structural analysis demonstrate that the former IL displays isotropic liquid phase behaviors, whereas the latter exhibits distinct ILC characteristics within a wide temperature range. All these computational results are essentially attributed to an alkyl chain length effect in $[C_2C_nIM]$ cations.

A sophisticated identification of smectic phase is complemented by analyzing number density distributions (Fig. 11), pair distribution functions (Fig. 12), orientational and translational order parameters (Fig. 13) of modelling systems. The number density profiles for CG beads in $[C_2C_{12}IM][BF_4]$ ILs at 300 K, as shown in Fig. 11(a), indicate a well-defined head-to-head and tail-to-tail crystalline pattern between ionic and hydrophobic layers with little overlap. The head CH and tail CT beads exhibit similar peak intensities but with displaced peak positions (Fig. 11(d)), and IM and BF beads have comparable density profiles (Fig. 11(c)) due to their strong coulombic interactions, as expected. An increase in temperature from 300 K leads to a considerable modulation of smectic phase

with boarder density distributions, which is quantitatively consistent with number density profiles of the corresponding atomistic reference groups in modelling systems at relevant thermodynamic states.^{72,73,78,79}

B. In-plane structures and dynamics

The descriptions of ILC and smectic phase structures of $[C_2C_4IM][BF_4]$, $[C_2C_{12}IM][BF_4]$, and $[C_2C_{20}IM][BF_4]$ ILs are complemented by in-plane pair distribution functions at xy plane perpendicular to phase director (z -axis). The $[C_2C_4IM][BF_4]$ IL is characterized by isotropic liquid structures, and therefore all in-plane RDFs (the first column in Fig. 12) exhibit mean distributions at all studied temperatures, which is not different from what usually observed in isotropic phase of ILs. However, the $[C_2C_{20}IM][BF_4]$ IL exhibits highly ordering in-plane structures consisting of alternating ion layering characteristics. The in-plane RDFs for charged beads (IM-IM, IM-BF, and BF-BF pairs) span beyond three nanometers, indicating a persistent modulation of long-ranged two dimensional ordering pattern as would be expected in a crystalline phase.^{79,80} The $[C_2C_{12}IM][BF_4]$ IL has intermediate in-plane structural properties consisting of alternating ion layers. The distributions of neutral CT beads in $[C_2C_{12}IM]$ cations are limited within few ionic radii and are consistent with a liquid-like structure of hydrophobic layers.

Fig. 13 presents orientational and translational order parameters of $[C_2C_nIM]$ cations to quantify their orientational and translational distributions in layering IL matrices. The orientational order parameter is defined as an ensemble average of the second-order Legendre polynomial, $S = \langle P_2(\cos \beta) \rangle$, where β is the angle between phase director (z -axis) and the directional vector pointing from head CH to tail CT beads in $[C_2C_nIM]$ cations.⁷⁸⁻⁸⁰ The orientational order parameters for cations with long alkyl chains, such as $[C_2C_{16}IM]$ and $[C_2C_{20}IM]$, are around 0.9 at low temperatures, indicating that these cations take uniform arrangements along the same direction in modelling systems. As temperature increases, molecular conformations of $[C_2C_nIM]$ cations become less orientationally ordered, corresponding to a solid-solid phase transition from crystalline to smectic A phase. This observation is generally consistent with

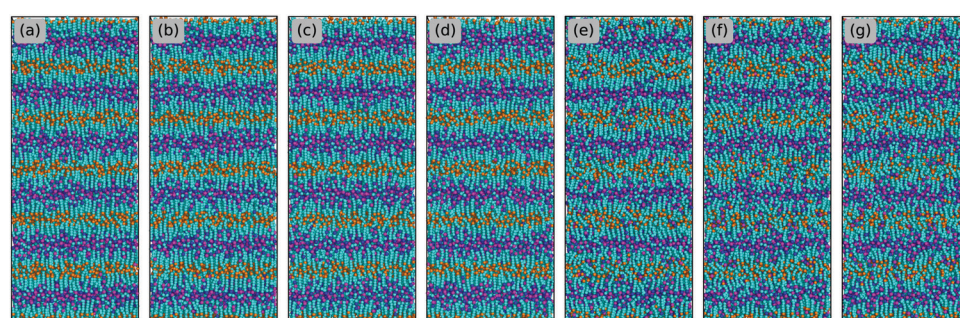


Fig. 10 Representative configurations of $[C_2C_{12}IM][BF_4]$ ILs in equilibrated simulation systems obtained from a sequential heating cascade. The tail CT beads in CG $[C_2C_{12}IM]$ cations are represented by orange spheres to highlight their spatial distributions in modelling systems and the formation of lamellae structures at low temperatures. (a-d) correspond to $[C_2C_{12}IM][BF_4]$ IL having crystalline phase at 100, 200, 300 and 350 K, (e and f) for IL having smectic phase at 400 and 450 K, and (g) for IL having quasi-smectic phase at 500 K.

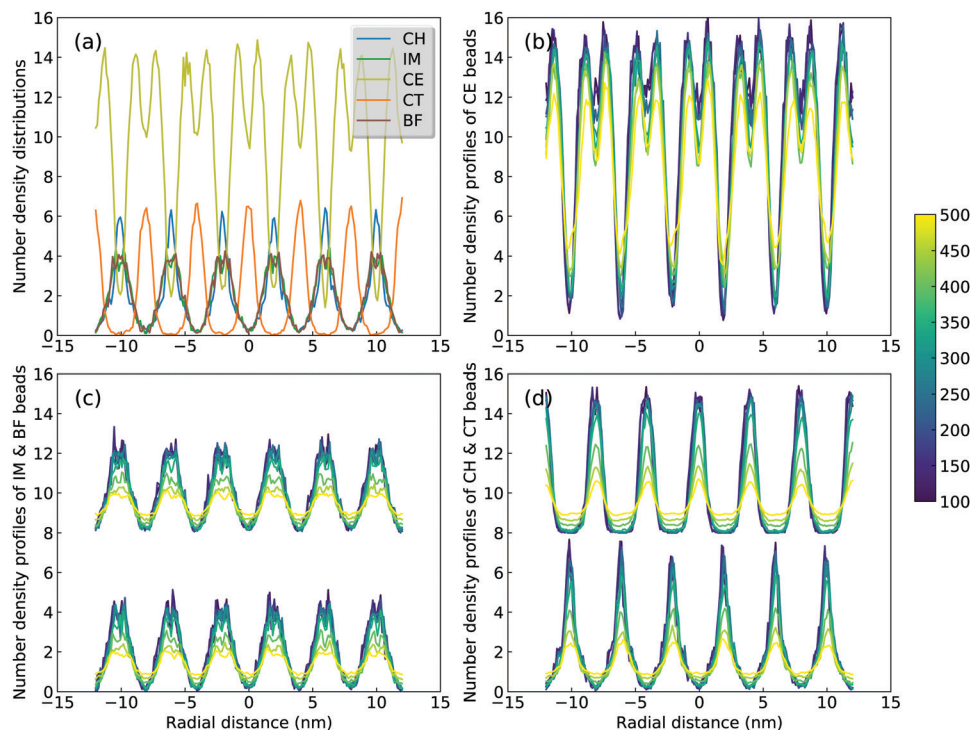


Fig. 11 Number density distributions of (a) CG beads in $[C_2C_{12}IM][BF_4]$ ILs along z -axis at 300 K, and of (b) CE, (c) IM and BF, and (d) CH and CT beads at different temperatures. The density profiles for BF and CT beads are vertically shifted by eight units for clarity.

experimental observations as these ILs indeed exhibit microstructural transitions with increasing temperatures.^{72,73} However, for cations having short alkyl chains, such as $[C_2C_2IM]$ and $[C_2C_4IM]$, the orientational order parameters are almost zero and do not show appreciable changes with decreasing temperatures, indicating that these simulation systems exhibit isotropic structures with minimal phase segregation between polar and apolar moieties, even at low temperatures. The orientational order parameters for cations with intermediate alkyl chains, like $[C_2C_{12}IM]$, lie between those for $[C_2C_8IM]$ and $[C_2C_{16}IM]$ ILs, and exhibit significant changes with temperatures. It is shown that at low temperatures, the orientational order parameters for $[C_2C_{12}IM]$ cations are close to 0.8, and present stepwise decrease from 100 to 350 K, and then an evident decrease at around 400 K. This indicates that microstructures in $[C_2C_{12}IM][BF_4]$ IL apparently lose crystalline mesomorphism and transform to smectic phase and then isotropic phase with less ordering characteristics, in which $[C_2C_{12}IM]$ cations are more interdigitated and alkyl chains exhibit more flexibilities with less spatial constraints than those exhibit aligned distributions at lower temperatures. This corresponds to a smectic-isotropic structural transition of $[C_2C_{12}IM][BF_4]$ IL as those observed in previous experiments and computational studies.^{72,73}

The translational order parameter τ is described by $\tau = \langle \cos(2\pi z/d) \rangle$, where z is the position of $[C_2C_nIM]$ cation beads along phase director, d is the layer spacing, and $\langle \rangle$ represents an ensemble average.^{73,80-82} It is shown in Fig. 13(b) that the translational order parameters for all modelling systems exhibit similar variations as orientational order parameters

with increasing temperatures. More pertinently, the translational order parameters for specific modelling systems at relevant temperatures are smaller than the corresponding orientational order parameters shown in Fig. 13(a), indicating that orientational distributions of $[C_2C_nIM]$ cations, either exhibiting crystalline, smectic mesomorphism, or isotropic nanosegregated structures, are somewhat significant compared with the corresponding translational distributions in characterizing phase structures of modelling systems, akin to that observed in CG MD simulations of ILs using a generic CG model represented by Gay–Berne potential.⁸²

It should be noted that herein we do not observe a sudden apparent jump in orientational and translational order parameters with increasing temperatures, which might be attributed to the simplified CG model for $[C_2C_nIM][BF_4]$ ILs.^{78,80} Although there are some discrepancies of transition temperatures between computational results and experimental observations due to some computational tricks, this does not prevent us from a qualitative understanding of experimental phenomena using CG MD simulations as the relative trends still provide insightful information on thermotropic phase behaviors of $[C_2C_nIM][BF_4]$ ILs at varied thermodynamic states. In addition, the comprehensive analysis of number density profiles, in-plane radial distribution functions, orientational and translational order parameters can provide further physical insights for microstructural transitions of $[C_2C_nIM][BF_4]$ ILs with a gradual lengthening of cation alkyl chains. The $[C_2C_nIM][BF_4]$ ILs with cation alkyl chains shorter than C_4 are isotropic liquids, whereas $[C_2C_nIM][BF_4]$ ILs with intermediate cation alkyl

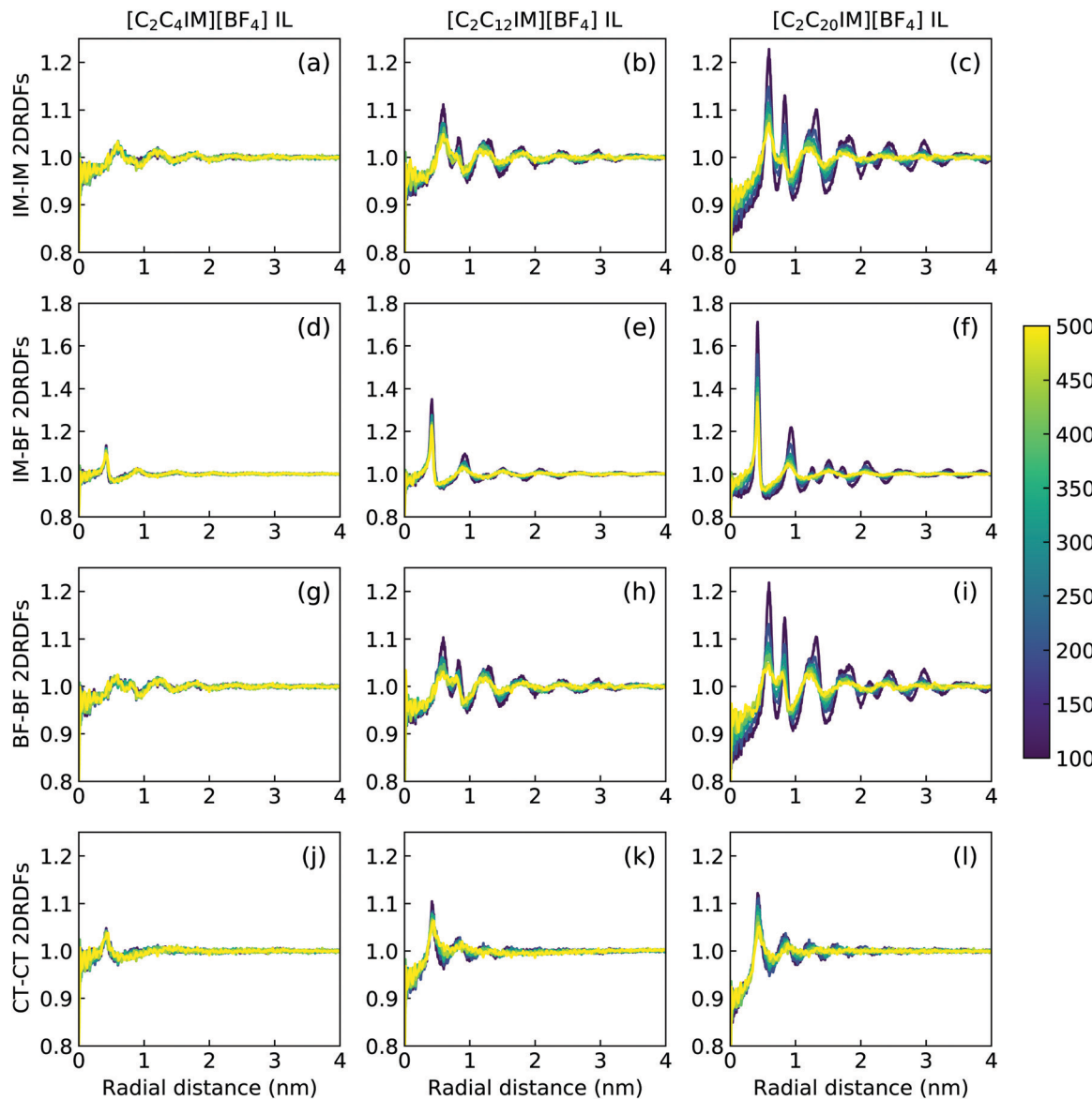


Fig. 12 In-plane radial distribution functions (2DRDFs) for IM–IM (the 1st row), IM–BF (the 2nd row), BF–BF (the 3rd row), and CT–CT (the 4th row) pairs in $[\text{C}_2\text{C}_4\text{IM}][\text{BF}_4]$ (the 1st column), $[\text{C}_2\text{C}_{12}\text{IM}][\text{BF}_4]$ (the 2nd column), and $[\text{C}_2\text{C}_{20}\text{IM}][\text{BF}_4]$ (the 3rd column) ILs at different temperatures.

chains ($4 < n < 12$) are heterogeneous liquids with a distinct segregation between polar and apolar domains. The spatial distributions of charged and neutral beads in these modelling systems do not allow a complete segregation of polar and apolar domains at mesoscopic level, which necessarily results in a perturbation of ion pairing interactions by alkyl chains, and *vice versa*.⁷⁸ A further lengthening of cation alkyl chains ($n \geq 12$) leads to their preferential alignments, in which polar and apolar domains are completely segregated, and as a consequence, ionic layers are not readily perturbed by long alkyl chains, which, however, have a significant effect on orientational ordering distributions of cations.⁷³

The microstructures of $[\text{C}_2\text{C}_n\text{IM}][\text{BF}_4]$ ILs, either characterized by crystalline, smectic mesomorphism, or isotropic nanosegregated structures, have a direct impact on translational mobilities of charged and neutral CG beads in modelling systems at different

temperatures. An increase in temperature leads to enhanced translational mobilities of CG beads with neutral spheres having larger diffusion coefficients ($D_{\text{CT}} > D_{\text{CE}} > D_{\text{CH}}$) than charged IM and BF beads at a wide temperature range, in which the latter two are strongly coupled *via* coulombic interactions, as shown in representative diffusion coefficient data for all CG beads in $[\text{C}_2\text{C}_{12}\text{IM}][\text{BF}_4]$ IL in Fig. 14(a).

Besides the total diffusion coefficients, the microstructures of $[\text{C}_2\text{C}_n\text{IM}][\text{BF}_4]$ ILs have additional effect on mobilities of CG beads at xy plane and along z -axis. Fig. 14(d) presents fractions of in-plane diffusion coefficient data of CG beads in $[\text{C}_2\text{C}_{12}\text{IM}][\text{BF}_4]$ IL over their counterparts along z -axis. The neutral beads have distinct mobilities at xy plane compared with their diffusions along z -axis owing to intrinsic crystalline structures of ILs at low temperatures, and such mobilities are significantly increased with temperatures due to their

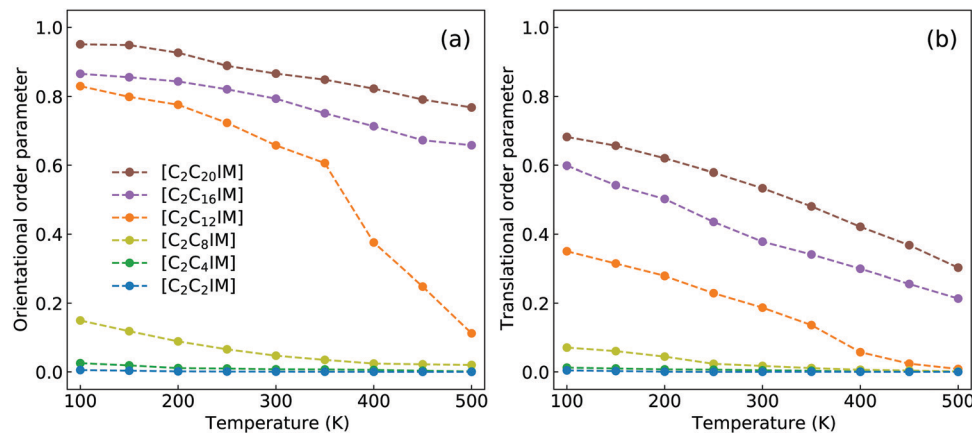


Fig. 13 Variations of (a) orientational and (b) translational order parameters for $[C_2C_nIM]$ cations at different temperatures.

enhanced in-plane diffusivities in apolar domains in modelling systems. The fractions for all CG beads are maximized at around 350 K, beyond which the values of D_{xy}/D_z decrease with increasing temperatures, which is rationalized by a phase transition of $[C_2C_{12}IM][BF_4]$ IL from crystalline mesomorphism to smectic and isotropic structures.

The variations of cation alkyl chains have a straightforward effect on in-plane mobilities of CG beads over their counterparts along z-axis, and representative results for charged IM beads and neutral CT spheres are present in Fig. 14(e) and (f), respectively. For cations with alkyl chains shorter than C_{12} , the in-plane mobilities of CG beads over their counterparts along z-axis are almost constant. This is expected as these ILs have homogeneous structures or form nanosegregated apolar domains within a framework consisting of charged beads but not smectic phase due to an imbalance of polar and apolar moieties in IL matrices. Therefore all CG beads in these

modelling systems, either charged IM (and BF) beads or neutral CT (also CH and CE) spheres, exhibit comparable mobilities in three dimensional space. However, for cations with alkyl chains longer than C_{12} , all CG beads exhibit enhanced diffusivities at xy plane over their counterparts along z-axis, in which neutral beads hold more significance than charged spheres due to intrinsic phase structures and specific distributions of these CG beads in modelling systems.

Dvinskikh and coworkers studied thermotropic phase behaviors of $[C_1C_{12}IM][BF_4]$ and $[C_1C_{12}IM]Br$ ILs and found heterogeneous mobilities of cations in ordered liquid environment characterized by smectic A phase.^{83,84} Compared with these experimental measurements, it is shown in Fig. 15 that the developed CG model for $[C_2C_nIM][BF_4]$ ILs can essentially capture heterogeneous diffusivities, including the total diffusion coefficients and the values of D_{xy}/D_z of $[C_2C_{12}IM]$ cations in varied thermodynamic and structural states. In addition, the

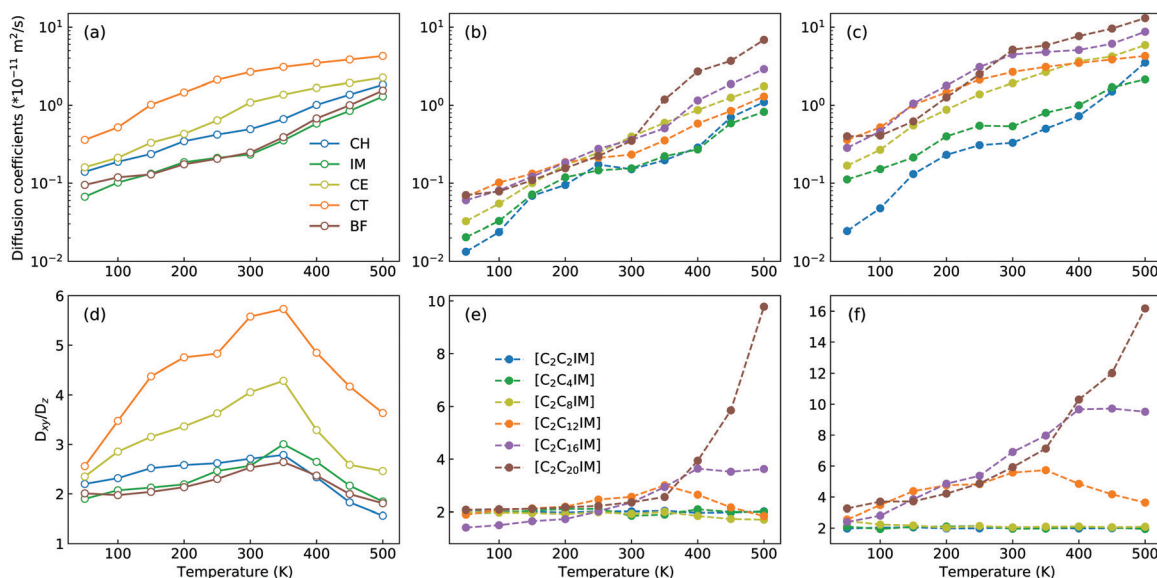


Fig. 14 Diffusion coefficient data of (a) CG beads in $[C_2C_{12}IM][BF_4]$ IL, and of (b) IM and (c) CT spheres in all six $[C_2C_nIM][BF_4]$ ILs at different temperatures. Fractions of in-plane diffusion coefficients (D_{xy}) over those along z-axis (D_z) of (d) CG beads in $[C_2C_{12}IM][BF_4]$ IL, and of (e) IM and (f) CT spheres in all six $[C_2C_nIM][BF_4]$ ILs at different temperatures.

experimental diffusion data for $[C_1C_{12}IM]Br$ IL at relevant temperatures are also provided in Fig. 15 for a comparative purpose. These comparisons demonstrate that the developed CG model can be specifically adopted to study thermodynamic and structural properties of ILs consisting of imidazolium cations coupled with spherical anions, and can be adapted to explore striking phase behaviors of other ILs consisting of cation having a polar head and hydrophobic tails coupled with anions characterized by different molecular shapes and sizes at varied thermodynamic states, which will be a central scheme for our computational studies in future.

IV. Ion association structures and ion hopping dynamics in polymerized ionic liquids

Imidazolium-based PILs are of interest as next-generation ion transport materials because of their particularities in combining mechanical stabilities of polymers with ion transport quantities of imidazolium ILs.^{7,22,23,25,31,85} Great endeavors have been focused on PILs where charged groups are pendant to polymer backbones. As PIL backbones and most pendant groups are apolar units, the charged moieties in cation monomers have strong coordinations with anions and form peculiar ionic aggregates, which has been observed in related experimental characterizations.^{23,28,86,87} The ensuing modelling works demonstrated that the formation of intriguing morphologies from spheres to strings of ionic aggregates depends on the degree of neutralization, ion types, and polymer architectures.^{32,36,88-90} It was further suggested that placing charged moieties in PIL backbones (ionenes) instead of pendant groups leads to the formation of substantially percolated ionic aggregates spanning the entire sample geometry, which has profound implications on ion conductivity and transport quantities of backbone PILs compared with their pendant analogous.^{28,31,88} Motivated by these reports, in the current study, we adopt the constructed CG model for $[C_2C_8IM]$ cation to probe structural and ion transport properties in a set of backbone and pendant polymerized

ionic liquids (labelled as BPILs and PPILs, respectively, and representative configurations of BPIL and PPIL chains are provided in Fig. 16) as previous CG MD simulations have demonstrated that $[C_2C_8IM][BF_4]$ IL exhibits distinct phase segregation between polar and apolar domains but without obvious IL crystalline mesomorphism. Backbone and pendant polymerized $[C_2C_8IM]$ cations are constructed with PIL backbone lengths ranging from 6 to 60 to explore the effects of PIL architectures and PIL molecular weights on ion mobilities and the mechanism underlying ion association structures and ion hopping dynamics in PIL materials. More specifically, a series of BPIL chains consisting of 1, 2, 3, 4, 5, 6, 8, and 10 $[C_2C_8IM]$ cation monomers with a head-to-tail polymerization manner is constructed, leading to BPIL backbones consisting of 6, 12, 18, 24, 30, 36, 48, and 60 CG beads (each $[C_2C_8IM]$ cation consists of 6 CG beads). Likewise, multiple PPIL chains are constructed in a head-to-head polymerization form with PPIL backbones containing 6, 12, 18, 24, 30, 36, 48, and 60 CH beads. Each modelling system contains 3600 $[C_2C_8IM][BF_4]$ ion pairs with different number of BPIL and PPIL chains. The detailed modelling protocols of BPIL and PPIL simulation systems are provided in ESI.†

A. Ion association structures

Fig. 16 presents representative morphologies and configurations of BPILs and PPILs in modelling systems. Both charged IM beads and tail CT spheres in $[C_2C_8IM]$ cations exhibit localized distributions in PPILs compared with their counterparts in BPILs, which can be rationalized by relative locations of IM and CT beads in PILs. In PPILs, the CH beads are covalently bonded together, leading to a close contact of IM beads. The strong electrostatic repulsions among charged IM beads result in a distinct aggregation of anions near IM beads to neutralize local charges, and therefore charged IM and BF beads exhibit distinct localizations in PPIL modelling systems (Fig. 16(b)). However, in BPILs, the charged IM beads are separated by five neutral beads, which can effectively reduce electrostatic repulsions between IM beads in neighboring $[C_2C_8IM]$ cation monomers, leading to the BPILs having coil-like structures in bulk regions. Such a distinct

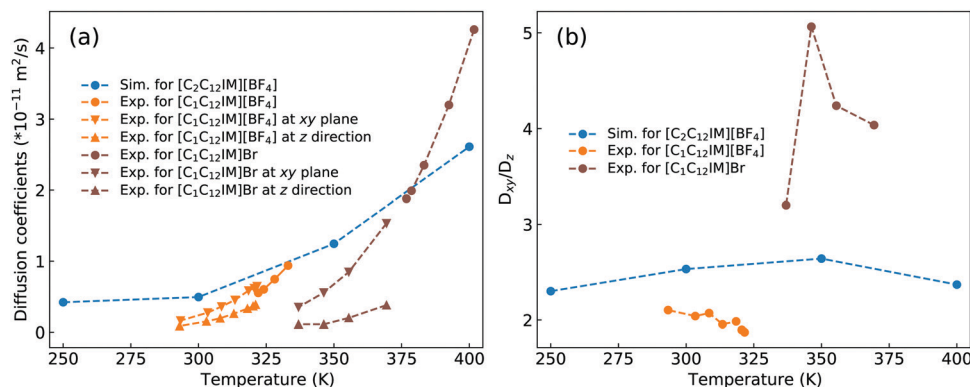


Fig. 15 Comparison of (a) the total diffusion coefficient data and (b) the fractions of in-plane diffusion coefficients (D_{xy}) over those along z -axis (D_z) of $[C_2C_{12}IM]$ cations in $[C_2C_{12}IM][BF_4]$ IL obtained from current CG MD simulations with experimental measurements of $[C_1C_{12}IM][BF_4]$ IL at relevant temperatures.⁸³ The experimental data for $[C_1C_{12}IM]Br$ IL at different temperatures are also provided for a comparative purpose.⁸⁴

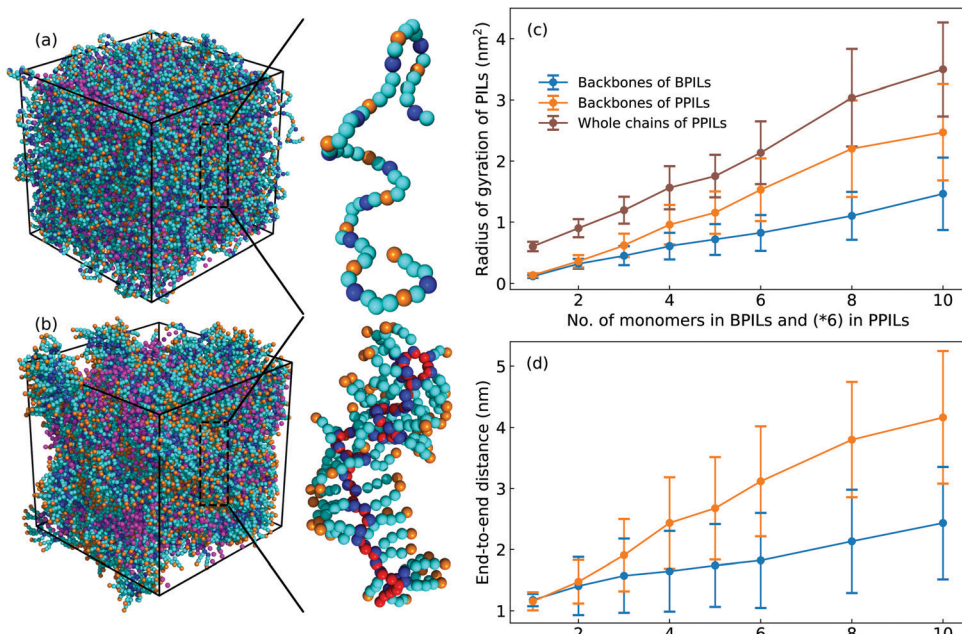


Fig. 16 Representative morphologies and configurations of (a) BPILs and (b) PPILs consisting of 10 and 60 $[C_2C_8M]$ cation monomers with comparable PIL backbone lengths, and variations of (c) radius of gyration and (d) end-to-end distance of BPILs and PPILs as a function of PIL backbone length. The tail CT beads in cation monomers in BPILs and PPILs, and the head CH beads in PPIL cation monomers are highlighted with orange and red spheres, respectively, to address their spatial distributions in modelling systems.

PIL architecture effect leads to varied conformational properties, such as radius of gyration (Fig. 16(c)) and end-to-end distance (Fig. 16(d)), of BPILs and PPILs, and thereafter results in striking ion transport properties that will be discussed in following paragraphs.

The local ion structures in BPILs and PPILs are qualitatively characterized by calculating radial distribution functions and the corresponding accumulated coordination numbers shown in Fig. 17. For CT-CT and IM-BF pairs, both BPILs and PPILs have similar cutoffs for the first solvation shell. However, a large coordination number is present for CT-CT and IM-BF pairs in PPILs compared with that in BPIL counterparts, indicating a preferential association between neutral CT beads of alkyl chains in apolar domains and a strong coordination between charged beads with unlike charges in polar domains, respectively, which are clearly visualized in Fig. 16. Such a strong coordination pattern between unlike charges leads to distinct correlations among charged beads with like charges.^{32,89} The BF-BF RDF plot has enhanced peak intensities at short radial distances in PPILs compared with that in BPILs, but with an almost equal probability for a central anion to coordinate with neighboring ones within the first solvation shell. The spacial correlations among neighboring IM beads exhibit a peculiar characteristic depending on PIL architectures. In PPILs, the IM-IM correlations have a small radius and thereafter a slightly reduced number of coordinating ions in the first solvation shell, whereas have a comparable radius but with a large number of coordinating ions in the second coordination shell in contrast to their analogues in BPILs. In addition, the out-of-phase feature at short distance in RDF plots is a ubiquitous

signature of charge alternation in ionic systems mediated by anions to neutralize cation charges, which may contribute to their varied capabilities in trapping charge carriers and thereafter affecting ion transport and hopping dynamics in BPILs and PPILs.

In order to have a comprehensive understanding of anion association patterns with neighboring polymerized cations, we have calculated the probability distribution for an anion to coordinate with n PIL cation monomers and with N PIL chains in BPILs and PPILs. An ion association state is defined for a specific ion pair with their relative distance smaller the cutoff of the first solvation shell in the corresponding RDF plot.^{30,32,36,89} It is displayed in Fig. 18(a) that the probabilities for anions in BPIL modelling systems exhibit sharply peaked distributions at $n = 4$, indicating a preferential coordination of an anion with four cation monomers in BPILs. However, a broad distribution with comparable probabilities centered at $n = 5$ and $n = 6$ corresponds to the most probable associations of an anion with approximately six cation monomers in PPIL modelling systems, which further confirms the localized coordination of anions with PPIL cation monomers in contrast to their associations with BPIL cation monomers.⁹⁰ It should be noted that these characteristics are invariant among BPILs and PPILs with different backbone lengths, as illustrated in Fig. 18(c), indicating that such a probability distribution represents an inherent coordination feature of an anion with four BPIL cation monomers and with six PPIL cation monomers in their respective modelling systems.

The associated characteristics of anions with PIL chains, as shown in Fig. 18(b), highlight significant variations for an

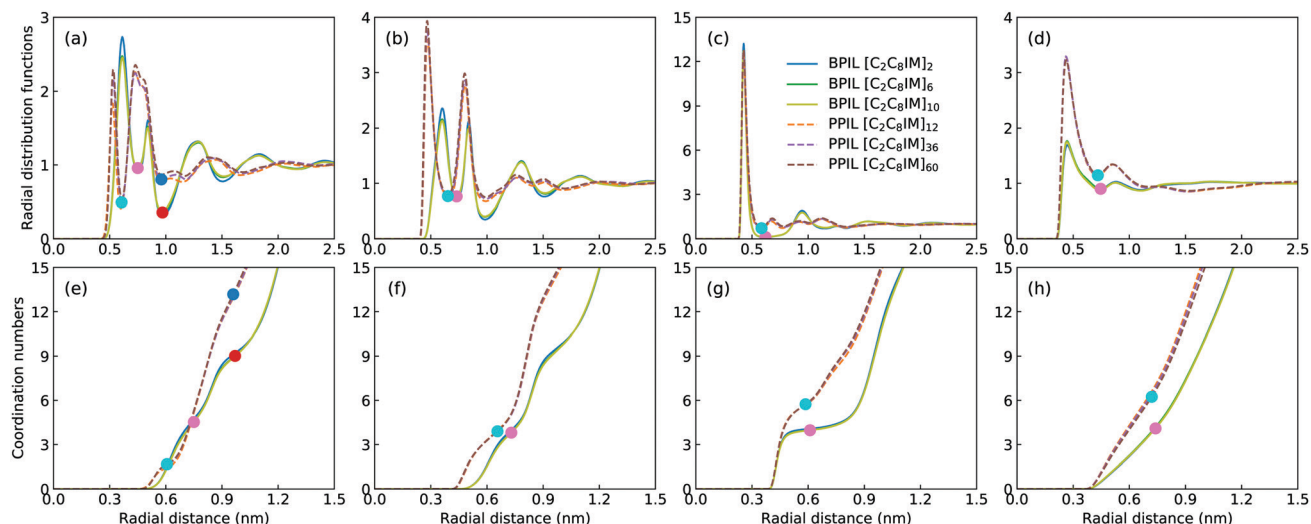


Fig. 17 Radial distribution functions (upper panels) and accumulated coordination numbers (lower panels) for (a and e) IM-IM, (b and f) BF-BF, (c and g) IM-BF, and (d and h) CT-CT pairs in representative BPILs and PPILs consisting of $[C_2C_8IM]$ cation monomers and $[BF_4]$ anions. The ● and ● spheres in all subfigures correspond to the first solvation shell for spatial distributions of specific beads around central ones in BPILs and PPILs, respectively. The ● and ● spheres in (a and e) panels represent the second coordination shell for spatial distributions of IM beads around central IM spheres in BPILs and PPILs, respectively.

anion to coordinate with different numbers of BPIL and PPIL chains. For monomeric $[C_2C_8IM][BF_4]$ IL, an anion exhibits its maximal coordination with four $[C_2C_8IM]$ cations. A head-to-tail polymerization manner of $[C_2C_8IM]$ cation monomers leads to a gradual shift of peak positions from $N = 4$ to $N = 3$, corresponding to a coordination pattern of an anion with fewer BPIL chains due to rigidity of BPIL backbones.⁹⁰ Such an associating state is also observed for PPILs with the most probably coordinated PPIL chains gradually shifted from $N = 2$ for PPILs with short backbones to $N = 1$ for PPILs with long backbones. These changes are clearly manifested in Fig. 18(c) addressing variations of the averaged numbers of associated PIL cation monomers and PIL chains per anion with a gradual lengthening of backbones in BPILs and PPILs.

The intra- and interchain coordinations between cation monomers in the first and second solvation shells, which are determined by the first and second minima in the corresponding RDF plots in Fig. 17, in BPILs and PPILs are illustrated in Fig. 19. All cations in monomeric IL matrix (BPIL with a

polymerization degree of 1) have interchain associations in the first and second solvation shells. Lengthening BPIL backbones leads to a considerable increase in intrachain coordinations for cation monomers (Fig. 19(a)), and a concomitant decrease in interchain associations from a maximal coordination probability with five interchain monomers to a maximal association probability with three interchain monomers (Fig. 19(b)). More specifically, for the BPIL with the polymerization degree equals to 10, it is shown that approximately 25% of cation monomer coordinations in the first solvation shell comes from intrachain associations, and the left 75% is described by interchain associations (Fig. 19(c)). Similar computational results are observed for associating BPIL cation monomers within the second solvation shell with comparable intra- and interchain contributions.

For intra- and interchain coordinations between cation monomers in PPILs, it is demonstrated that almost all PPIL cation monomers have intrachain associations with neighboring ones in the first solvation shell (Fig. 19(a)), and these

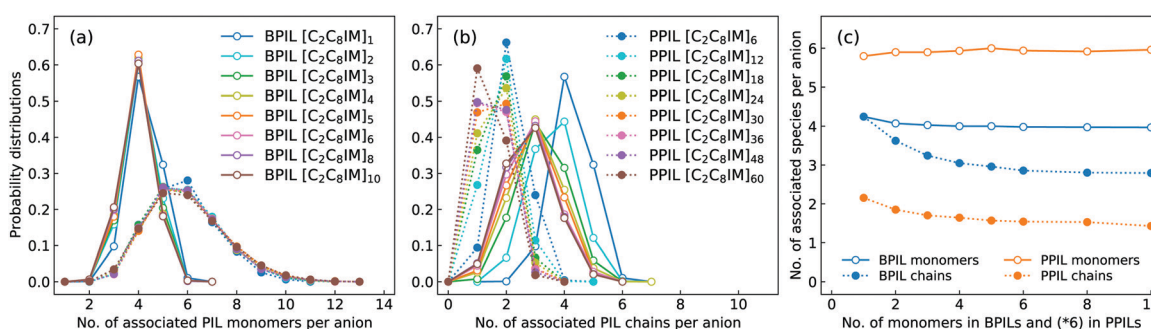


Fig. 18 Probability distributions of coordination numbers of an anion in associating (a) PIL cation monomers and (b) PIL chains, and (c) the averaged coordination numbers of associated PIL cation monomers and PIL chains with one anion in BPILs and PPILs with varied PIL backbone lengths.

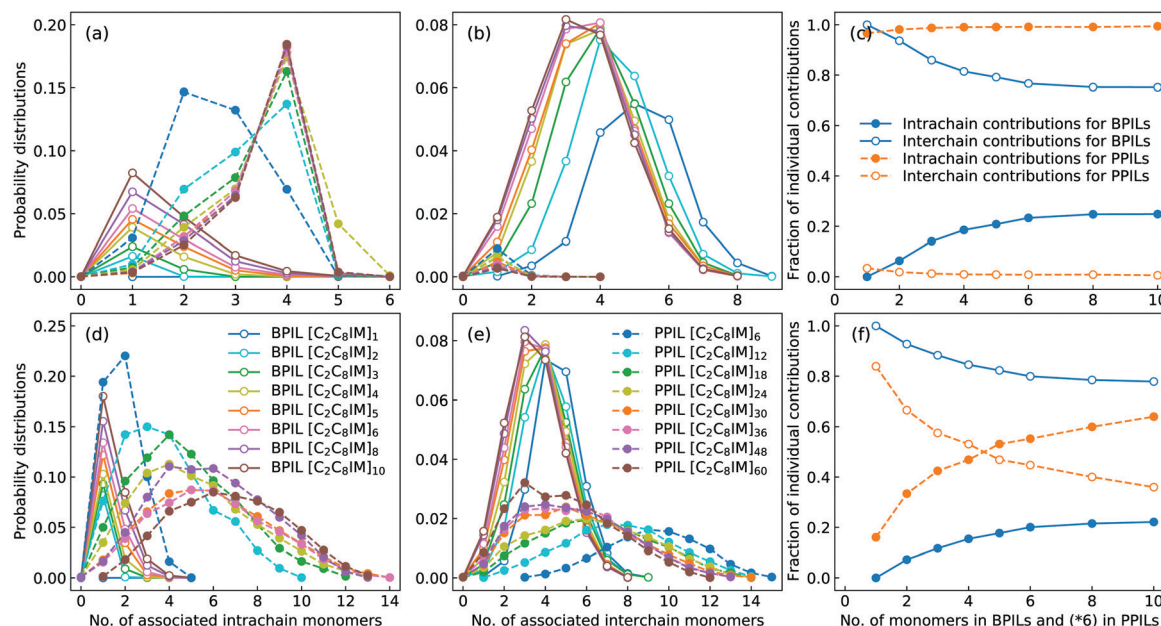


Fig. 19 Probability distributions of coordination numbers of associated (a and d) intra- and (b and e) interchain cation monomers, and (c and f) fractions of their individual contributions to the total number of associated cation monomers in the first (upper panels) and second (lower panels) solvation shells in BPILs and PPILs.

associations exhibit a substantial shift of maximal distribution from $n = 2$ for $[\text{C}_2\text{C}_8\text{IM}]_6$ PPIL to $n = 4$ for $[\text{C}_2\text{C}_8\text{IM}]_{60}$ PPIL with a gradual lengthening of PPIL backbones.^{91,92} Meanwhile, intrachain coordinations between PPIL cation monomers in the second solvation shell exhibit a gradual transition from a sharp probability distribution localized at $n = 2$ to that characterized by broad distributions centered at around $n = 6$ (Fig. 19(d)), and a concomitant shift for maximal interchain associations from $n = 10$ to $n = 3$ (Fig. 19(e)). The individual contributions of intrachain coordinations between PPIL cation monomers in the second solvation shell are increased from 16% for $[\text{C}_2\text{C}_8\text{IM}]_6$ PPIL to 64% for $[\text{C}_2\text{C}_8\text{IM}]_{60}$ PPIL, and correspondingly, the contributions of interchain coordinations are gradually decreased from 84% to 36% with a gradual lengthening of PPIL backbones (Fig. 19(f)). Such a spatial constraint of anions around cation monomers in PPILs, on the one hand, leads to their decreased diffusions in PPILs, and on the other hand, may

have a significant effect on the mobility of other charge carriers, such as lithium ions in lithium salt-doped PPILs which are promising electrolyte materials for batteries, supercapacitors, and other electrochemical devices.

B. Ion hopping dynamics

The diffusion coefficients of cation monomers and anions as shown in Fig. 20(a) demonstrate that these ion groups exhibit enhanced mobilities in BPILs compared with their counterparts in PPILs due to distinct spatial constraints of anions around PPIL cation monomers. More pertinently, both cation monomers and anions exhibit monotonic decrease in their mobilities with a gradual lengthening of BPIL and PPIL backbones, and concomitantly, BPILs and PPILs have reduced ion conductivities (Fig. 20(b)) and enhanced anion transference numbers (Fig. 20(c)).

Based on a systematic analysis of ion association structures and ion diffusivities, we proceed to examine different ion

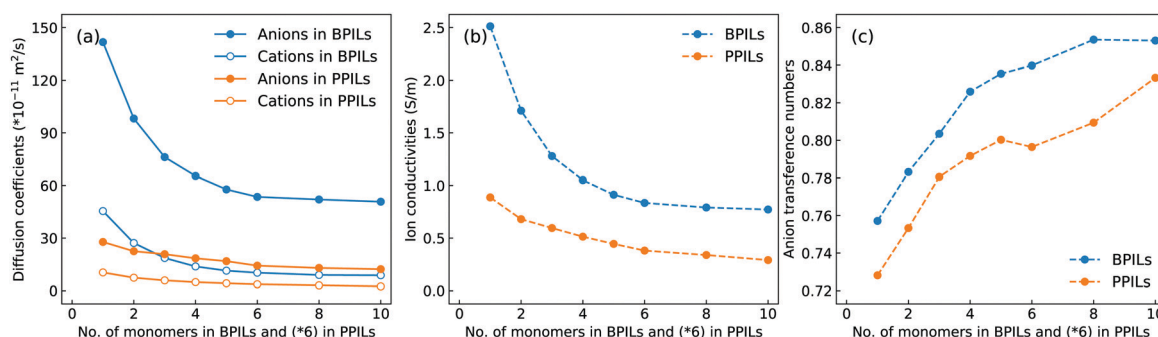


Fig. 20 (a) Diffusion coefficients of cation monomers and anions, (b) ion conductivities, and (c) anion transference numbers in BPILs and PPILs with varied PIL backbone lengths.

hopping features and their variations with lengthening backbones in BPILs and PPILs. An ion hopping event is considered to occur when an ion pair association breaks or a new association forms.^{30,32,36,90} With identifications of associated anions with PIL cation monomers, the anion hopping events can be classified into four distinct types that are sketched in Fig. 21. The type I is termed as rattling hopping, where anions are associated with the same cation monomers within a time interval Δt . The type II is labelled as intrachain hopping, in which anions are associated with different cation monomers in the same PIL chains before and after Δt . The type III is described as interchain hopping, where anions are associated with cation monomers in different PIL chains as time elapses from $t = 0$ to $t = \Delta t$. The type IV is tagged as nonassociated hopping, in which anions are transitioned from associated to nonassociated states within Δt . The fractions of these four ion hopping types in BPILs and PPILs are illustrated in Fig. 21(e) and (f), respectively.

A substantial fraction of rattling hopping (type I) is observed, making up of approximately 20% and 42% in BPILs and PPILs, respectively, indicating that a considerable amount of anions do not experience breaking or forming of ion pairing associations within a time interval Δt . Such a striking feature for rattling hopping is even more distinct in PPILs compared

with that in BPILs, owing to peculiar ion pairing associations of anions with cation monomers that have been rationalized by RDFs and accumulated coordination numbers shown in Fig. 17 and by ion associating probability distributions present in Fig. 18. This leads to enhanced probabilities of intrachain hopping (type II) in PPILs, which is roughly 52% of the total anion hopping events compared with that of 22% in BPILs. For interchain hopping (type III) of anions in BPILs and PPILs, a common feature is that such a hopping event has less probabilities with a gradual lengthening of PIL backbones, whereas a different character is that in BPILs this hopping mode is overwhelmingly dominant compared with other hopping modes and in PPILs this hopping type is progressively replaced by rattling and intrachain hopping modes. It is noted that the probability for nonassociated ion hopping event is essentially negligible, which is attributed to strong associations among anions and cation monomers in BPILs and PPILs *via* decisive coulombic interactions.

The detailed analyses of ion associations between anions and cation monomers and anion hopping modes in BPILs and PPILs indicate that PIL architectures indeed have a significant effect on ion transport quantities in PIL materials. To quantify correlations of ion diffusivities with ion structural relaxation times and ion association lifetimes, we calculate continuous

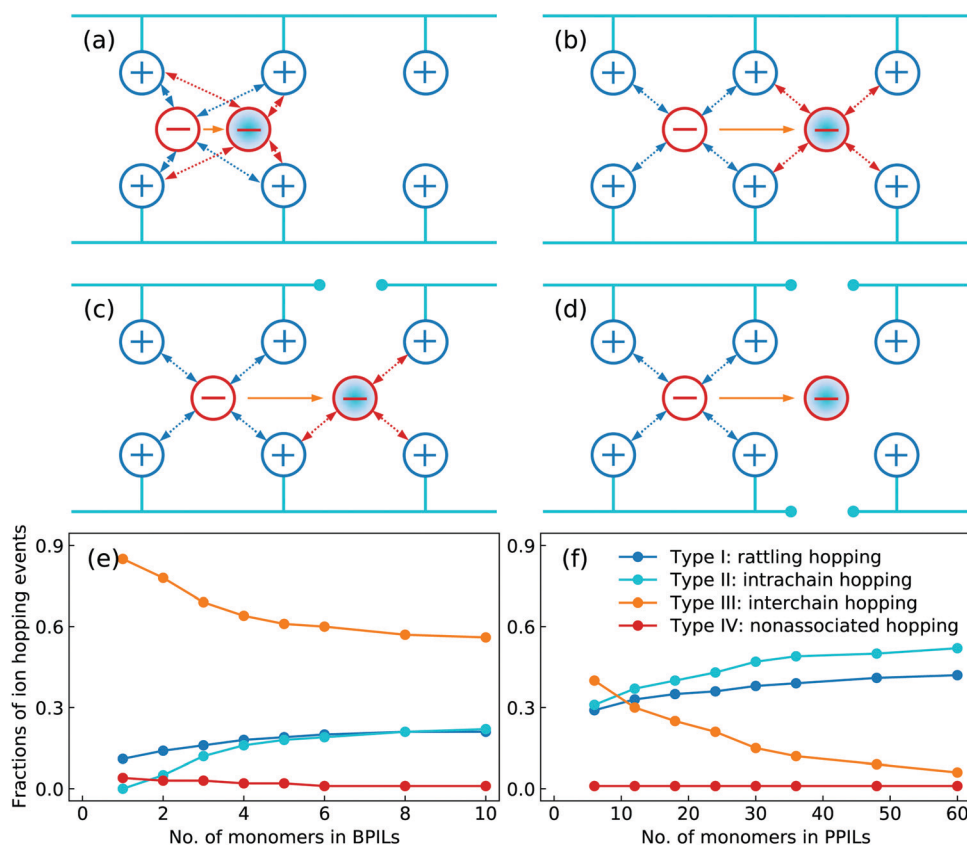


Fig. 21 Definition of ion hopping types to distinguish anion hopping events in BPILs and PPILs with varied backbone lengths. (a) type I: rattling hopping, (b) type II: intrachain hopping, (c) type III: interchain hopping, and (d) type IV: nonassociated hopping. The orange arrows denote anion mobility from $t = 0$ (open red circles) to $t = \Delta t$ (blue-filled red circles), and the blue dotted arrows and red dotted arrows correspond to coordinations of anions with cation monomers at $t = 0$ and $t = \Delta t$, respectively. Fractions of different ion hopping types in (e) BPILs and (f) PPILs with varied backbone lengths.

ion pairing correlation function, $S(t) = \frac{\langle H(t)h(0) \rangle}{\langle h \rangle}$, and intermittent ion pairing correlation function, $C(t) = \frac{\langle h(t)h(0) \rangle}{\langle h \rangle}$, in which $h(t)$ is assigned to unity if an ion pairing association is present at $t = 0$ and remains intact at time t , and $H(t)$ has a value of unity if an ion pairing coordination that exists at $t = 0$ remains intact continuously up to time t .^{32,36,90} Therefore, $S(t)$ measures continuous ion pairing coordinations and $C(t)$ describes intermittent ion structural associations before their permanent dissociations, and the corresponding time scales, τ_S and τ_C , quantifies the average lifetimes of ion pairing coordinations and ion structural relaxations, respectively. τ_S and τ_C can be derived by fitting the corresponding correlation functions, $S(t)$ and $C(t)$, respectively, to stretched exponential functions and thereafter integrating the fitted analytical forms.

Fig. 22 presents diffusion coefficients of PIL cation monomers and anions against ion pairing association times (τ_S) and ion structural relaxation times (τ_C). It is clearly demonstrated that diffusion coefficients of ion species are inversely correlated with their relaxation times and follow a universal power law correlation of $D \sim \tau^{-1}$, indicating an intrinsic correlation of ion diffusivities and ion hopping dynamics with ion pairing associations and ion structural relaxations in PILs, irrespective of PIL architectures. This observation is generally consistent with atomistic computational results from previous works.^{30,32,36,90} Recalling that $S(t)$ decays with an initial breaking of cation–anion ion pairing coordinations and $C(t)$ decays with a final dissociation of cation–anion ion structural associations, it can be conceptually addressed that τ_S should be comparable with the time scale for rattling hopping mode (type I) as both quantities reflect an instant breaking of ion pairing coordinations. This rattling hopping mode does not contribute to effective ion transport, but is an indicative of probability of ion pairing dissociation. A small τ_S (fast decay of $S(t)$) corresponds to an associated ion pair that can be readily dissociated in a short time interval. Such an ion

dissociation probability can be substantially increased *via* external stimuli, such as introduction of inorganic salts or imposing external electric field for specific applications of BPILs and PPILs as electrolyte materials in electrochemical devices. $C(t)$ is intrinsically correlated with ion “caging” effect constraining a vibrational motion of associated or semi-associated ion pairs in local ionic environment before their final dissociation, and therefore τ_C is an appropriate index to describe effective ion hopping dynamics (types II and III, and even type IV) and their lifetimes in modelling systems.

V. Concluding remarks and outlook

In this work we have constructed a novel CG model for $[C_2C_nIM][BF_4]$ ILs with cation alkyl chains up to C_{20} to study phase behaviors of monomeric and polymeric ILs with different architectures. The interaction parameters for this CG model were validated against representative thermodynamics (liquid densities), structural (radial distribution functions and probability distributions of bond lengths, angles and dihedrals), and dynamic properties (diffusion coefficients) that were obtained from atomistic reference simulations and experimental measurements at relevant thermodynamic states.

This constructed CG model was adopted to study thermotropic characteristics of monomeric ILs with varied cation alkyl chains. A structural evolution from homogeneous to nano-segregated liquid structures and then a smectic crystalline mesomorphism was identified *via* a gradual lengthening of cation alkyl chains from C_2 to C_{20} . In addition, a systematic structural analysis (density profiles, in-plane pair distribution functions, diffusion coefficients, orientational and translational order parameters) illustrates a distinct structural transition in a sequential heating cascade characterized by a monotonic decrease in orientational order parameters, which is qualitatively consistent with experimental thermotropic phase behaviors of ILCs at a wide temperature range.

This CG model was further extended to explore ion association structures and the molecular mechanism underlying ion hopping phenomena in BPILs and PPILs with different PIL backbone lengths. Anions demonstrate comparable probabilities to coordinate with PIL cation monomers, but striking association features with PIL chains. PIL cation monomers illustrate distinct intra- and interchain coordinations depending on specific PIL architectures and spatial distributions of cation monomers around reference units, leading to a substantial decrease in ion transport properties and anion hopping dynamics with a gradual lengthening of PIL backbones. A considerable amount of anions has local rattling hopping inside ion cages without cation–anion association breaking and reforming, whereas significant differences manifest that lengthening PIL backbones leads to a progressive increase in anion intrachain ion hopping probabilities and a concomitant decrease in anion interchain ion hopping events, underscoring a PIL architecture effect as that hypothesized in previous atomistic simulations. Ion diffusivities of PIL cation monomers

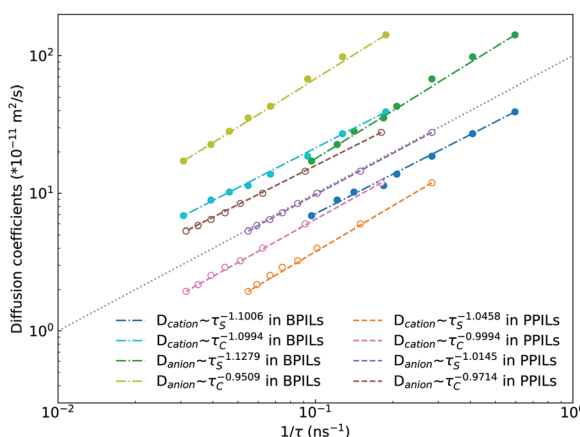


Fig. 22 Diffusion coefficients of PIL cation monomers (D_{cation}) and anions (D_{anion}) against ion pairing association times (τ_S) and ion structural relaxation times (τ_C). The dotted grey line with a slope of 1 represents a guide to the eye.

and anions are inversely correlated with ion pairing association lifetimes and ion structural relaxation times *via* a universal power law correlation $D \sim \tau^{-1}$, irrespective of PIL architectures, mirroring qualitatively the ion hopping interpretation of ion conductivity data for PILs in earlier experimental and computational investigations.

Altogether, these computational studies of thermotropic phase behaviors of monomeric ILs with varied cation alkyl chains and of ion association and transport properties in BPILs and PPILs indicate that the constructed CG model for $[C_2C_nIM][BF_4]$ ILs and the derived interaction parameters are effective in reproducing relevant properties of IL-based materials at different thermodynamic states and providing physical insights in local ion association structures and ion hopping dynamics in PIL materials. It is expected that such a CG model will be a generic bead-spring model representing a series of IL-based materials having different ion structures and varied polymer architectures, and is adequate to reveal molecular-level quantities underlying peculiar structure–property relationships for ion-containing (polymeric) materials. This will be of particular significance for building a library of specific structure–property ontology and for a systematic computational design of novel ion-containing materials at mesoscopic level to meet specific requirements in electrochemical applications.

Conflicts of interest

There are no conflicts to declare.

Acknowledgements

Y.-L. W. acknowledges financial support from Knut and Alice Wallenberg Foundation (KAW 2018.0380) and partial support from Swedish Research Council. B. L. acknowledges financial support from National Natural Science Foundation of China (No. 22003080), and Fundamental Research Funds for Central Universities (No. 20lgpy76). A. L. acknowledges Swedish Research Council for financial support, and partial support from Ministry of Research and Innovation of Romania (CNCS – UEFISCDI, project number PN-III-P4-ID-PCCF-2016-0050, within PNCDI III). We thank Prof. Jiayin Yuan in Stockholm University for insightful discussion. These computations were enabled by resources provided by Swedish National Infrastructure for Computing (SNIC) at PDC, HPC2N, and NSC partially funded by Swedish Research Council through grant agreement no. 2016-07213.

References

- 1 E. W. Castner Jr, C. J. Margulis, M. Maroncelli and J. F. Wishart, *Annu. Rev. Phys. Chem.*, 2011, **62**, 85.
- 2 R. Hayes, G. G. Warr and R. Atkin, *Chem. Rev.*, 2015, **115**, 6357.
- 3 D. Bedrov, J.-P. Piquemal, O. Borodin, A. D. MacKerell Jr, B. Roux and C. Schroder, *Chem. Rev.*, 2019, **119**, 7940.
- 4 Y.-L. Wang, B. Li, S. Sarman, F. Mocci, Z.-Y. Lu, J. Yuan, A. Laaksonen and M. D. Fayer, *Chem. Rev.*, 2020, **120**, 5798.
- 5 M. Armand, F. Endres, D. R. MacFarlane, H. Ohno and B. Scrosati, *Nat. Mater.*, 2009, **8**, 621.
- 6 F. Zhou, Y. Liang and W. Liu, *Chem. Soc. Rev.*, 2009, **38**, 2590.
- 7 D. R. MacFarlane, M. Forsyth, P. C. Howlett, M. Kar, S. Passerini, J. M. Pringle, H. Ohno, M. Watanabe, F. Yan and W. Zheng, *et al.*, *Nat. Rev. Mater.*, 2016, **1**, 15005.
- 8 Z. Zhang, J. Song and B. Han, *Chem. Rev.*, 2016, **117**, 6834.
- 9 J. Y. Shin, S. A. Yamada and M. D. Fayer, *J. Am. Chem. Soc.*, 2017, **139**, 11222.
- 10 K. Goossens, P. Nockemann, K. Driesen, B. Goderis, C. Görller-Walrand, K. Van Hecke, L. Van Meervelt, E. Pouzet, K. Binnemans and T. Cardinaels, *Chem. Mater.*, 2008, **20**, 157.
- 11 D. A. Turton, J. Hunger, A. Stoppa, G. Hefter, A. Thoman, M. Walther, R. Buchner and K. Wynne, *J. Am. Chem. Soc.*, 2009, **131**, 11140.
- 12 S.-C. Luo, S. Sun, A. R. Deorukhkar, J.-T. Lu, A. Bhattacharyya and I. J. Lin, *J. Mater. Chem.*, 2011, **21**, 1866.
- 13 K. Goossens, K. Lava, C. W. Bielawski and K. Binnemans, *Chem. Rev.*, 2016, **116**, 4643.
- 14 Y. Nozaki, K. Yamaguchi, K. Tomida, N. Taniguchi, H. Hara, Y. Takikawa, K. Sadakane, K. Nakamura, T. Konishi and K. Fukao, *J. Phys. Chem. B*, 2016, **120**, 5291.
- 15 Y. Wang and G. A. Voth, *J. Am. Chem. Soc.*, 2005, **127**, 12192.
- 16 A. Triolo, O. Russina, H.-J. Bleif and E. Di Cola, *J. Phys. Chem. B*, 2007, **111**, 4641.
- 17 D. W. Bruce, C. P. Cabry, J. N. Canongia Lopes, M. L. Costen, L. D'Andrea, I. Grillo, B. C. Marshall, K. G. McKendrick, T. K. Minton and S. M. Purcell, *et al.*, *J. Phys. Chem. B*, 2017, **121**, 6002.
- 18 J. Haddad, D. Pontoni, B. M. Murphy, S. Festersen, B. Runge, O. M. Magnussen, H.-G. Steinrück, H. Reichert, B. M. Ocko and M. Deutscher, *Proc. Natl. Acad. Sci. U. S. A.*, 2018, **115**, E1100.
- 19 Y. Ji, R. Shi, Y. Wang and G. Saielli, *J. Phys. Chem. B*, 2013, **117**, 1104.
- 20 G. Casella, V. Causin, F. Rastrelli and G. Saielli, *Liq. Cryst.*, 2016, **43**, 1161.
- 21 J. Sakuda, M. Yoshio, T. Ichikawa, H. Ohno and T. Kato, *New J. Chem.*, 2015, **39**, 4471.
- 22 J. Yuan, D. Mecerreyes and M. Antonietti, *Prog. Polym. Sci.*, 2013, **38**, 1009.
- 23 W. Qian, J. Texter and F. Yan, *Chem. Soc. Rev.*, 2017, **46**, 1124.
- 24 M. Watanabe, M. L. Thomas, S. Zhang, K. Ueno, T. Yasuda and K. Dokko, *Chem. Rev.*, 2017, **117**, 7190.
- 25 S.-Y. Zhang, Q. Zhuang, M. Zhang, H. Wang, Z. Gao, J.-K. Sun and J. Yuan, *Chem. Soc. Rev.*, 2020, **49**, 1726.
- 26 J.-H. Choi, Y. Ye, Y. A. Elabd and K. I. Winey, *Macromolecules*, 2013, **46**, 5290.
- 27 J. R. Sangoro, C. Iacob, A. Agapov, Y. Wang, S. Berdzinski, H. Rexhausen, V. Strehmel, C. Friedrich, A. Sokolov and F. Kremer, *Soft Matter*, 2014, **10**, 3536.

28 C. M. Evans, C. R. Bridges, G. E. Sanoja, J. Bartels and R. A. Segalman, *ACS Macro Lett.*, 2016, **5**, 925.

29 C. Iacob, A. Matsumoto, M. Brennan, H. Liu, S. J. Paddison, O. Urakawa, T. Inoue, J. Sangoro and J. Runt, *ACS Macro Lett.*, 2017, **6**, 941.

30 S. Mogurampelly, J. R. Keith and V. Ganesan, *J. Am. Chem. Soc.*, 2017, **139**, 9511.

31 P. Kuray, T. Noda, A. Matsumoto, C. Iacob, T. Inoue, M. A. Hickner and J. Runt, *Macromolecules*, 2019, **52**, 6438.

32 X. Luo, H. Liu and S. J. Paddison, *ACS Appl. Polym. Mater.*, 2021, **3**, 141.

33 J. R. Sangoro and F. Kremer, *Acc. Chem. Res.*, 2012, **45**, 525.

34 Z. Wojnarowska, J. Knapik, J. Jacquemin, S. Berdzinski, V. Strehmel, J. Sangoro and M. Paluch, *Macromolecules*, 2015, **48**, 8660.

35 J. Bartels, G. E. Sanoja, C. M. Evans, R. A. Segalman and M. E. Helgeson, *Macromolecules*, 2017, **50**, 8979.

36 Z. Zhang, B. K. Wheatle, J. Krajniak, J. R. Keith and V. Ganesan, *ACS Macro Lett.*, 2019, **9**, 84.

37 R. Yan, M. Antonietti and M. Oschatz, *Adv. Energy Mater.*, 2018, **8**, 1800026.

38 F. Fan, W. Wang, A. P. Holt, H. Feng, D. Uhrig, X. Lu, T. Hong, Y. Wang, N.-G. Kang and J. Mays, *et al.*, *Macromolecules*, 2016, **49**, 4557.

39 W. Zhao, F. Leroy, B. Heggen, S. Zahn, B. Kirchner, S. Balasubramanian and F. Müller-Plathe, *J. Am. Chem. Soc.*, 2009, **131**, 15825.

40 Y. Zhang and E. J. Maginn, *J. Phys. Chem. Lett.*, 2015, **6**, 700.

41 Y.-L. Wang, *J. Phys. Chem. B*, 2018, **122**, 6570.

42 B. Bhargava and M. L. Klein, *Soft Matter*, 2009, **5**, 3475.

43 J. Yuan, S. Soll, M. Drechsler, A. H. Müller and M. Antonietti, *J. Am. Chem. Soc.*, 2011, **133**, 17556.

44 Y. Wang, S. Izvekov, T. Yan and G. A. Voth, *J. Phys. Chem. B*, 2006, **110**, 3564.

45 M. Salanne and Phys Chem, *Chem. Phys.*, 2015, **17**, 14270.

46 A. Moradzadeh, M. H. Mottevaselian, S. Y. Mashayak and N. R. Aluru, *J. Chem. Theory Comput.*, 2018, **14**, 3252.

47 F. Uhlig, J. Zeman, J. Smiatek and C. Holm, *J. Chem. Theory Comput.*, 2018, **14**, 1471.

48 Y.-L. Wang, Y.-L. Zhu, Z.-Y. Lu and A. Laaksonen, *Soft Matter*, 2018, **14**, 4252.

49 D. Roy, N. Patel, S. Conte and M. Maroncelli, *J. Phys. Chem. B*, 2010, **114**, 8410.

50 Y. Wang, S. Feng and G. A. Voth, *J. Chem. Theory Comput.*, 2009, **5**, 1091.

51 H. A. Karimi-Varzaneh, F. Müller-Plathe, S. Balasubramanian and P. Carbone, *Phys. Chem. Chem. Phys.*, 2010, **12**, 4714.

52 D. Roy and M. Maroncelli, *J. Phys. Chem. B*, 2010, **114**, 12629.

53 C. Merlet, M. Salanne, B. Rotenberg and P. A. Madden, *J. Phys. Chem. C*, 2011, **115**, 16613.

54 C. Merlet, M. Salanne and B. Rotenberg, *J. Phys. Chem. C*, 2012, **116**, 7687.

55 C. Merlet, B. Rotenberg, P. A. Madden, P.-L. Taberna, P. Simon, Y. Gogotsi and M. Salanne, *Nat. Mater.*, 2012, **11**, 306.

56 C. Péan, C. Merlet, B. Rotenberg, P. A. Madden, P.-L. Taberna, B. Daffos, M. Salanne and P. Simon, *ACS Nano*, 2014, **8**, 1576.

57 Y.-L. Wang, A. Lyubartsev, Z.-Y. Lu and A. Laaksonen, *Phys. Chem. Chem. Phys.*, 2013, **15**, 7701.

58 A. Lyubartsev, A. Mirzoev, L. Chen and A. Laaksonen, *Faraday Discuss.*, 2010, **144**, 43.

59 O. Y. Fajardo, S. Di Lecce and F. Bresme, *Phys. Chem. Chem. Phys.*, 2020, **22**, 1682.

60 L. I. Vazquez-Salazar, M. Selle, A. H. De Vries, S. J. Marrink and P. C. Souza, *Green Chem.*, 2020, **22**, 7376.

61 Y.-L. Wang, *J. Phys. Chem. B*, 2020, **124**, 7452.

62 P. Kebelinski, J. Eggebrecht, D. Wolf and S. Phillpot, *J. Chem. Phys.*, 2000, **113**, 282.

63 K. R. Harris, M. Kanakubo and L. A. Woolf, *J. Chem. Eng. Data*, 2006, **51**, 1161.

64 J. Salgado, T. Regueira, L. Lugo, J. Vijande, J. Fernández and J. Garca, *J. Chem. Thermodyn.*, 2014, **70**, 101.

65 D. Song and J. Chen, *J. Chem. Eng. Data*, 2014, **59**, 257.

66 H. Tokuda, K. Hayamizu, K. Ishii, M. A. B. H. Susan and M. Watanabe, *J. Phys. Chem. B*, 2004, **108**, 16593.

67 I. Skarmoutsos, T. Welton and P. A. Hunt, *Phys. Chem. Chem. Phys.*, 2014, **16**, 3675.

68 Z. Hu and C. J. Margulis, *Proc. Natl. Acad. Sci. U. S. A.*, 2006, **103**, 831.

69 J. J. Hettige, J. C. Araque, H. K. Kashyap and C. J. Margulis, *J. Chem. Phys.*, 2016, **144**, 121102.

70 B. Wu, J. P. Breen and M. D. Fayer, *J. Phys. Chem. C*, 2020, **124**, 4179.

71 K. V. Axenov and S. Laschat, *Materials*, 2011, **4**, 206.

72 M. E. Di Pietro, T. Margola, G. Celebre, G. De Luca and G. Saielli, *Soft Matter*, 2019, **15**, 4486.

73 W. Cao, B. Senthilkumar, V. Causin, V. P. Swamy, Y. Wang and G. Saielli, *Soft Matter*, 2020, **16**, 411.

74 Y. V. Nelyubina, A. S. Shaplov, E. I. Lozinskaya, M. I. Buzin and Y. S. Vygodskii, *J. Am. Chem. Soc.*, 2016, **138**, 10076.

75 T. Li, F. Xu and W. Shi, *Chem. Phys. Lett.*, 2015, **628**, 9.

76 A. Erbas and M. O. De La Cruz, *Phys. Chem. Chem. Phys.*, 2016, **18**, 6441.

77 G. Saielli and Y. Wang, *J. Phys. Chem. B*, 2016, **120**, 9152.

78 W. Cao, Y. Wang and G. Saielli, *J. Phys. Chem. B*, 2018, **122**, 229.

79 G. Saielli, *J. Phys. Chem. B*, 2016, **120**, 2569.

80 G. Saielli, *Soft Matter*, 2012, **8**, 10279.

81 M. Bates and G. Luckhurst, *J. Chem. Phys.*, 1999, **110**, 7087.

82 G. Saielli, T. Margola and K. Satoh, *Soft Matter*, 2017, **13**, 5204.

83 M. Cifelli, V. Domenici, B. B. Kharkov and S. V. Dvinskikh, *Mol. Cryst. Liq. Cryst.*, 2015, **614**, 30.

84 D. Majhi, J. Dai, A. V. Komolkin and S. V. Dvinskikh, *Phys. Chem. Chem. Phys.*, 2020, **22**, 13408.

85 D. Mecerreyes, *Prog. Polym. Sci.*, 2011, **36**, 1629.

86 U. H. Choi, Y. Ye, D. Salas de la Cruz, W. Liu, K. I. Winey, Y. A. Elabd, J. Runt and R. H. Colby, *Macromolecules*, 2014, **47**, 777.

87 Y. Shao, Y.-L. Wang, X. Li, A. K. Kheirabad, Q. Zhao, J. Yuan and H. Wang, *Angew. Chem., Int. Ed.*, 2020, **59**, 17187.

88 L. M. Hall, M. J. Stevens and A. L. Frischknecht, *Phys. Rev. Lett.*, 2011, **106**, 127801.

89 J. R. Keith, N. J. Rebello, B. J. Cowen and V. Ganesan, *ACS Macro Lett.*, 2019, **8**, 387.

90 J. R. Keith and V. Ganesan, *J. Chem. Phys.*, 2019, **151**, 124902.

91 J. R. Keith, S. Mogurampelly, F. Aldukhi, B. K. Wheatle and V. Ganesan, *Phys. Chem. Chem. Phys.*, 2017, **19**, 29134.

92 Q. Zhao and C. M. Evans, *Macromolecules*, 2021, **54**, 3395.